Permeability and Porosity of Loose Granular Salt

Report to
Sandia National Laboratories

From
Department of Civil, Construction and Environmental Engineering
University of New Mexico

October 5, 2022

This report is derived directly from the thesis of Evan Babcock, who received an MS degree in Civil Engineering from the University of New Mexico in August, 2022 under the supervision of Professor John Stormont.

ABSTRACT

In this study, permeability and porosity measurements are made and reported for loose granular salt from the Waste Isolation Pilot Plant (WIPP). Measurements are made on a particularly wide range of particle sizes of this salt in a permeameter constructed large enough to fit and represent mixtures containing salt particles up to 25.4 cm in size. Salt samples with different particle size distributions are constructed and tested at varying levels of consolidation due to induced vibrations. Permeability measurements are made at a varying range of porosities for a given sample. Measurements are also compared with a predictive model for permeability of porous media to further evaluate the results of this study. The permeabilities measured in this study are within an order of magnitude to the predictions made by the model. Adjustments for settling and instability are also made to the model to better predict permeability measurements.

TABLE OF CONTENTS

ABSTRACT ii

TABLE OF CONTENTS iii

LIST OF FIGURES x

LIST OF TABLES xii

1. INTRODUCTION AND BACKGROUND 1

1.1 The Nuclear Waste Problem 1

1.2 Salt as a Repository 1

1.3 The WIPP Facility 3

1.4 Roof Falls at WIPP 4

1.4.1 Roof Fall Occurrences 4

1.4.3 Why Roof Falls are a Problem 12

1.5 Roof Fall Material Permeability and Porosity 15

1.5.1 Existing Data on Granular Salt 15

1.5.2 Why Not Field Measurements? 15

1.5.3 Predictive Models (K/C) 16

1.5.4 Considerations for Laboratory Tests on Rubble 17

1.6 Objectives 18

2. MATERIALS AND METHODS 19

2.1 Summary 19

2.2 Salt Used to Create Samples 19

2.3 Grain Size Distributions 22

2.3.1 Processing the Rubble Material 22

2.3.2 Processing the ROM Material 23

2.3.3 Rubble and ROM Grain Size Distributions 24

2.4 Large-Scale Permeameter/Porosimeter 25

2.4.1 Experimental Configuration 25

2.4.2 Rigid Box 28

2.4.3 Plastic and Neoprene Sheeting 30

2.4.4 Manifolds 31

2.4.5 Vacuum Source 32

2.4.6 Reservoir 32

2.4.7 Flow Measurements 32

2.4.8 Pressure Measurements 33

2.4.9 Tubing/Piping 34

2.4.10 Experimental Procedure for Measuring Permeability 34

2.4.11 Experimental Procedure for Measuring Porosity 35
2.5 Permeability and Porosity Interpretation 36
2.5.1 Permeability Interpretation 36
2.5.2 Porosity Interpretation 38
2.6 Small-Scale Verification Tests 40
2.6.1 Reasoning for Verification Tests 40
2.6.2 General Experimental Configuration 41
2.7 Resolution of Measurements 43
2.8 Test Conduct 43
2.8.1 Densification 44
2.8.2 Samples and Test Conditions 44
3. RESULTS AND DISCUSSION 47
3.1 Permeability vs. Porosity Results 47
3.1.1 Data Included 47
3.1.2 Error Bars 48
3.2 Discussion of Results 49
3.2.1 ROM Tests Indicate Permeability Increases as Porosity Increases 49
3.2.2 ROM Samples Have Lower Permeability Than Samples Which Include Rubble 49
3.2.3 Difference Between Small and Large-Scale Measurements on ROM 50

4. ANALYSIS 52

4.1 Permeability vs. Porosity Relationship with Grain Size Distribution: Kozeny-Carman 52

4.1.1 Carrier Interpretation of KC 53

4.1.2 Limitations and Suggestions for Improvement 55

4.2 Stability Analysis 59

4.2.1 Kenny and Lau Theory and Derivation 59

4.2.2 Unstable Particle Sizes 60

4.3.3 Unstable Particle Removal 61

5. CONCLUSION 63

5.1 Experimental Configuration Development 63

5.2 Permeability and Porosity Relationship 64

5.2.1 What Trends Are Observed in This Relationship? 64

5.2.2 KC Predictive Model Results 65

5.3 Future Work 65

5.3.1 Further Analysis of Results and Models 65

5.3.2 Analysis of CT Images 66

5.3.3 Large-Scale Permeability Testing with Vertical and Horizontal Flow 66

5.3.4 Diffusion Testing 67

6. APPENDICES 68

A: Unsuccessful Sample Information 69

B: Exact Permeability and Porosity Measurements 72

C: Non-linear Flow Correction Plots for Permeability Measurements 74

D: Kenny and Lau Stability Analysis Results 83

7. REFERENCES 87

LIST OF FIGURES

Figure 1: Roof fall aftermath 5

Figure 2: Stratigraphy at waste storage room depth 7

Figure 3: Sliding movement at Seam B and MB139 layer discontinuities 9

Figure 4: Sequence from corner stress crack propagation to roof collapse 11

Figure 5: Schematic representation of room closure over time 12

Figure 6: Human intrusion scenario 14

Figure 7: ROM salt upon arrival at UNM 20

Figure 8: Intact 30-cm -diameter solid rock salt core 21

Figure 9: Quartering the flattened cone of ROM salt 23

Figure 10: Comparison of the grain size distributions for ROM and Rubble salt 24

Figure 11: Permeameter schematic cross section 26

Figure 12: Photo of permeameter 27

Figure 13: Top view photo of partially filled permeameter 28

Figure 14: Small-Scale Permeameter schematic 41

Figure 15: Photo of the Small-Scale Permeameter 42

Figure 16: Permeability vs. porosity relationship 47

Figure 17: Schematic of layering 51

Figure 18: Permeability vs. porosity data with Kozeny-Carman predictive model 55

Figure 19: Permeability vs. porosity data with adjusted Kozeny-Carman predictive model 58

Figure 20: KC predictive model with all particles determined to be unstable removed 61

Figure 21: Non-linear flow correction for ROM 2 before shaking..... 74

Figure 22: Non-linear flow correction for ROM 2 after shaking 75

Figure 23: Non-linear flow correction for ROM 3 before shaking..... 76

Figure 24: Non-linear flow correction for ROM 3 after shaking 77

Figure 25: Non-linear flow correction for Small-Scale 1 before shaking 78

Figure 26: Non-linear flow correction for Small-Scale 1 after shaking 78

Figure 27: Non-linear flow correction for Small-Scale 1 after reset and before shaking..... 79

Figure 28: Non-linear flow correction for Small-Scale 1 after reset and after shaking..... 80

Figure 29: Non-linear flow correction for Small-Scale 1 after reset and after shaking twice..... 80

Figure 30: Non-linear flow correction for Rubble 5 before shaking 81

Figure 31: Non-linear flow correction for Rubble 5 after shaking 82

Figure 32: Non-linear flow correction for Rubble 8..... 82

Figure 33: Kenny and Lau stability analysis plot for 100% ROM. 83

Figure 34: Kenny and Lau stability analysis plot for 20% Rubble..... 84

Figure 35: Kenny and Lau stability analysis plot for 40% Rubble..... 85

Figure 36: Kenny and Lau stability analysis plot for 70% Rubble..... 86

LIST OF TABLES

Table 1: WIPP Salt Samples Tested and Their Key Parameters..... 46

Table 2: Removal of Fines from the KC Model Prediction..... 59

Table 3: Unsuccessful WIPP Salt Samples Tested and Their Key Parameters 69

Table 4: Successful Permeability and Porosity Measurements Made 72

1. INTRODUCTION AND BACKGROUND

1.1 The Nuclear Waste Problem

As transuranic nuclear waste began to accumulate during the mid-twentieth century from defense and energy activities, the United States government became focused on its safe disposal. Transuranic (TRU) waste is defined as waste contaminated with transuranic elements such as plutonium and other synthetically produced, radioactive elements having an atomic number greater than uranium (United States Nuclear Regulatory Commission n.d.). TRU waste is of concern because it is hazardous and long-lived. TRUs contain Plutonium-239, which has a half-life of 24,000 years. Many other TRU elements also have half-lives over 1000 years. TRU waste can be very hazardous to human health. As the fatal whole-body dose for humans is approximately 500 rem all at once, clearly even trace amounts of this waste, such as found on rags or clothing for example, is a serious health concern (United States Nuclear Regulatory Commission n.d.). Due to TRU waste's uniquely long-term and detrimental potential threats to public and environmental health, it's clear the issue of disposal required special attention.

1.2 Salt as a Repository

In 1957, it was recommended by the National Academy of Sciences that radioactive waste be disposed of in "*cavities mined in salt beds and salt domes,"* (NAS, 1957). Salt beds offer several advantages for disposal of TRU waste. First, salt beds are typically found in locations with very little seismic activity, making them relatively stable to contain the waste for its particularly long radioactive lifetime. Second, salt beds are free of flowing water since they

are nearly impermeable in their in-situ state. The extremely low permeability limits scenarios where contaminants can be transported through the salt to overlying water-bearing zones or to the surface. Third, salt has a high thermal conductivity. This is important due to the possibility of any increase in temperature after disposal. Build-up of heat causes gas contained in confined pores to become pressurized. Since the salt can transfer heat easily away from the heat source, pressure build-ups are far less likely to occur. Finally, rock salt is plastic, causing it to flow and heal its own fractures. This "viscoplastic" behavior is expected to cause the salt to slowly deform into the mined areas where TRU waste is placed, effectively encapsulating the waste in the impermeable salt (WIPP Site n.d.).

The United States is not the only country interested in utilizing bedded salt formations as a repository for TRUs. The German government and researchers began collaborations with the United States in the 1970s as both governments were exploring salt as an option for disposal of TRUs and High-Level Waste (HLW) (Hansen et al., 2017). While the US salt disposal research program has fluctuated over time principally due to political considerations, the Germans have continued to focus their radioactive waste disposal research on bedded salt among other geologic media.

Salt has been successfully used in the United States for other energy related activities aside from waste disposal. The Strategic Petroleum Reserve (SPR) was established in 1975 to develop an emergency stockpile of crude oil (Energy.gov 2015). In 1977, underground salt domes along the Gulf Coast of the United States were selected as storage sites and the first shipment of crude oil from Saudi Arabia was received to be stored. Domal salt is similar to bedded salt in that they are both relatively impermeable and plastic. The fact that salt domes are

much more economical in storing oil than tanks due to the ease of salt mining was a principal reason the SPR was placed in salt formations. Since salt is relatively impermeable compared to other subterranean geological formations (being much easier to mine than formations of similar permeabilities), and the plastic properties of the salt seal any fractures in the surrounding salt, crude oil leaks are very unlikely (Energy.gov 2015).

Additionally, underground salt caverns have been used for storage of hydrogen. As hydrogen gas becomes a more cost-effective alternative energy source, an economical means of storage for the gas is necessary. Chevron Phillips has used salt caverns and domes in Texas to store hydrogen since the 1980s (AIS Software 2017). The success of underground salt formations in storing hydrogen is due to many of the same reasons for its success in storing petroleum. Salt's self-healing properties are especially valuable in maintaining the low permeability of the salt, which isolates the hydrogen from the environment and limits loss of product.

1.3 The WIPP Facility

Twenty-six miles southeast of Carlsbad in southeastern New Mexico lies a 600-meter-deep salt bed layer produced by prehistoric evaporation cycles. In 1979, Congress approved this location as the site of the Waste Isolation Pilot Plant (WIPP). TRU waste produced by national defense activities was first disposed of at WIPP in 1999. Owned and operated by the Nuclear Waste Partnership (NWP) LLC. US DOE, WIPP is the only TRU waste disposal facility in the United States, and disposes of radioactively contaminated wastes including laboratory clothing, debris, residues, soil, etc. (WIPP Site n.d.).

At 655-meters below ground surface, WIPP lies in the Permian salt deposits in the Delaware Basin. These deposits compose several horizontally bedded salt layer formations made up of halite, anhydrite, dolomite, and siltstone (Powers et al., 1978). WIPP disposal rooms are in the Salado Formation, which is made up of relatively pure salt layers and has 300-meters of salt layers isolating them from above sedimentary layers, and 600-meters of salt layers isolating them from limestone layers below (The Current Bases for Roof Fall Prediction at WIPP and a Preliminary Prediction for SPDV Room 2 1993). Excavation of storage rooms began in 1986, but excavations for the Site Preliminary Design Validation (SPDV) program began in 1983. SPDV rooms and current storage rooms are 4.6 meters in height, 11 meters wide, and 100 meters in length and grouped in arrays with 33-meter-thick walls separating each other.

1.4 Roof Falls at WIPP

1.4.1 Roof Fall Occurrences

Large, unsupported rooms have been observed to experience roof collapses, such as the collapse of SPDV Room 1 8-years after its excavation. Roof collapses are typically triangular cross sections along nearly the entire room length which fall several meters to the ground, creating piles of salt rubble as shown in Figure 1. These roof collapses are expected over time without proper management (i.e., bolting), and because of the viscoplastic nature of the surrounding salt, rooms are eventually expected to close-up and entomb contained waste while also reconsolidating salt rubble (Reedlunn et al., 2019).



Figure 1: Roof fall aftermath salt rubble (Reedlunn et al., 2019)

The factors involved in causing roof falls are complex. An important consideration for roof falls is the composition and stratigraphy of the bedded salt formation in which the rooms are excavated. The Salado Formation is made up of relatively pure salt (halite) layers, but with notable layers of anhydrite, polyhalite, and clay including thin clay seams (Stormont 1990). Three clay seams are observed in the immediate vicinity of the repository rooms as shown in Figure 2. Approximately 4 meters above the roof exists a 20-cm layer of anhydrite underlain by a thin clay seam. Additionally, 2 meters of relatively pure halite separate the room horizon from what is defined as “Seam B”, which consists of a 10 cm thick layer of anhydrite underlain by a

clay seam. Finally, approximately 1.4 meters of salt separates the room floor from a 70 cm thick layer of anhydrite and polyhalite defined as Marker Bed 139 (MB139), which is also underlain by a clay seam (The Current Bases for Roof Fall Prediction at WIPP and a Preliminary Prediction for SPDV Room 2 1993). While these clay seams are no more than a couple of centimeters thick, they have very low shear and tensile strength relative to the surrounding rock salt.

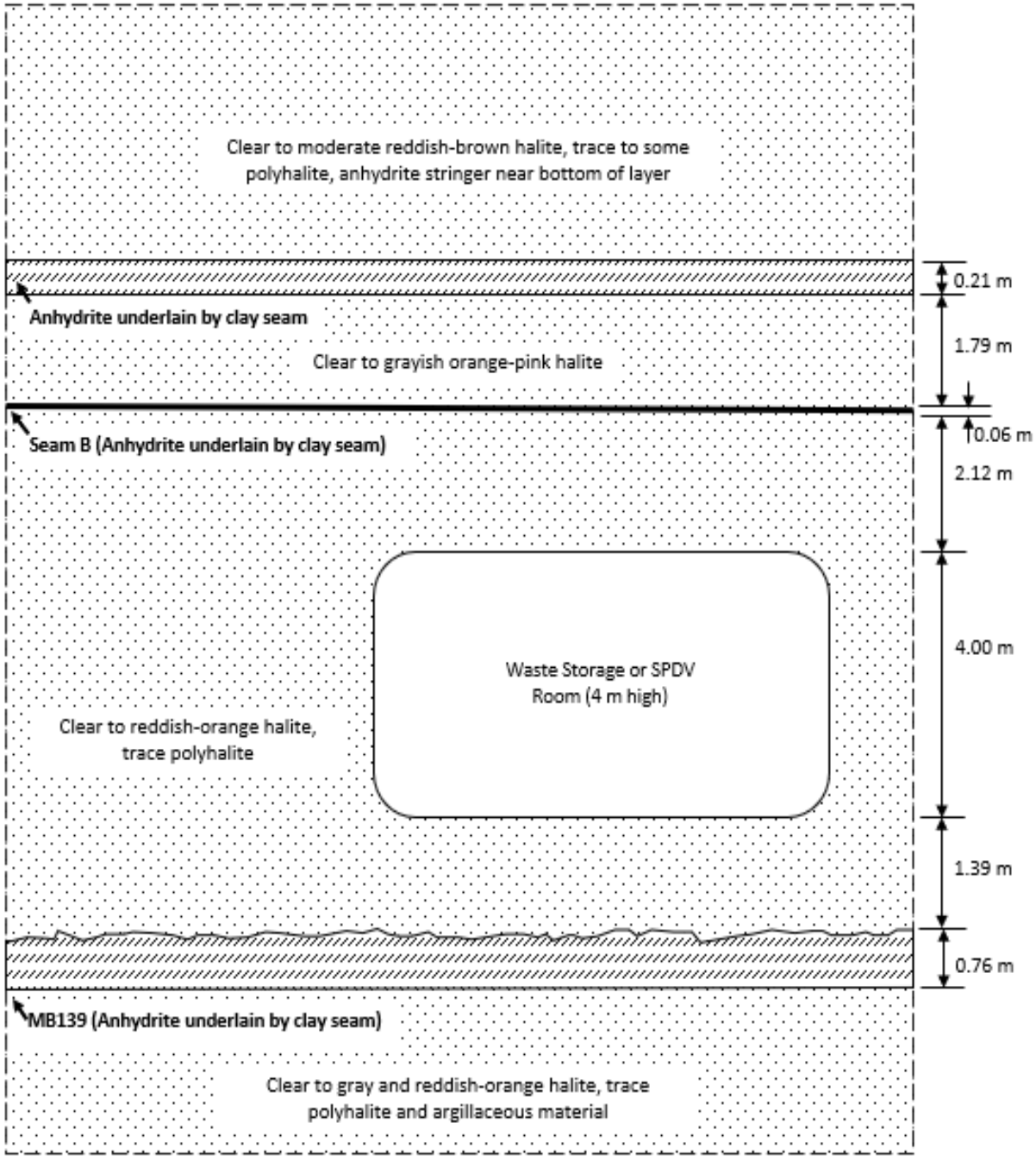

Figure 2: Stratigraphy at waste storage room depth. Three clay seams in immediate vicinity of rooms. [Adapted from Borns and Stormont (1988)]

In 1983, SPDV test rooms were excavated and installed with an extensive array of geotechnical monitoring instruments including boreholes for extensometers, inclinometers, and gas-flow/permeability measurements. Seismic tomography and refraction equipment was also employed for further analysis. Measurements indicated movement of bedded salt layers along both Seam B and MB139 as illustrated in Figure 3. The 2-meter-thick salt layer between the room horizon and Seam B can be thought of as a roof beam while the 1.4 m salt layer between the room floor and MB139 can be thought of as a floor beam. Monitoring instruments revealed that in SPDV Room 1, horizontal fracturing as well as differential vertical and horizontal movements in the roof beam began not long after excavation. In 1988, it became clear that the horizontal fractures above the roof beam were propagating and connecting, creating widespread separation of the roof beam from overlying layers at Seam B. As borings were made along the length of the roof beam, dust from drilling was observed at borings up to 10 meters from the boring being drilled, revealing the length of the fractured spaces above the roof beam. Room 1 was then evacuated and barricaded in May 1989 (The Current Bases for Roof Fall Prediction at WIPP and a Preliminary Prediction for SPDV Room 2 1993). In February 1991, the roof collapsed.

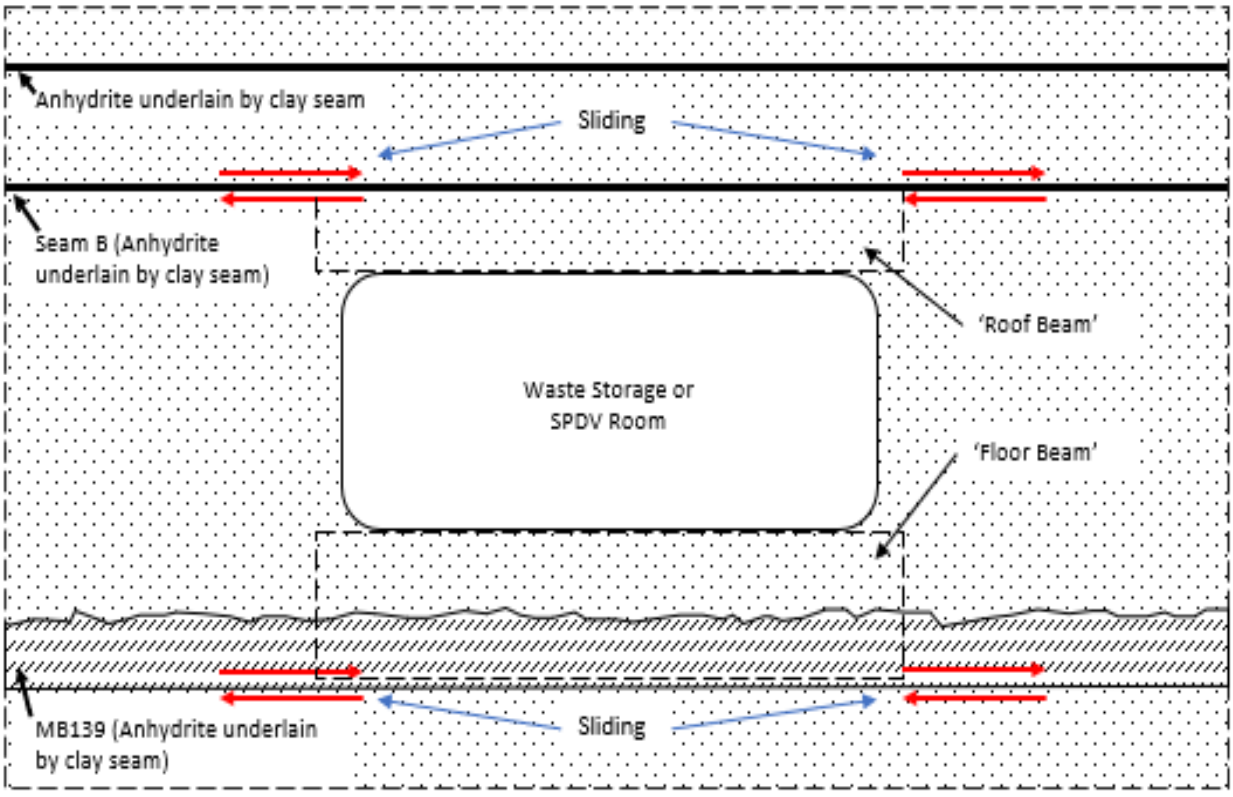

Figure 3: Sliding movement at Seam B and MB139 layer discontinuities [Adapted from (The Current Bases for Roof Fall Prediction at WIPP and a Preliminary Prediction for SPDV Room 2 1993)].

The discontinuous behavior of the surrounding salt formation is the main cause of the fracturing and strains observed to lead to roof collapse. Large geologic stresses due to the subsurface depth of the salt formation result in large compressive stresses on the roof beam which is created by the plane of shear weakness at Seam B (Figure 3). These compressive stresses cause the roof beam to deform and creep to the center of excavations. Vertical creep due to geologic pressures and roof beam self-weight generate intense stresses at the corners of rooms

and at the ends of the roof beam. These relatively large corner stresses cause fracturing to occur as shown in Figure 4a. These fractures propagate to the seams of shear weakness and connect causing large disconnections of the roof beam at Seam B shown in Figure 4b. Finally, prolonged deviatoric creep stresses cause fractures to worsen over time and eventually cause the room roofs to collapse (Figure 4c).

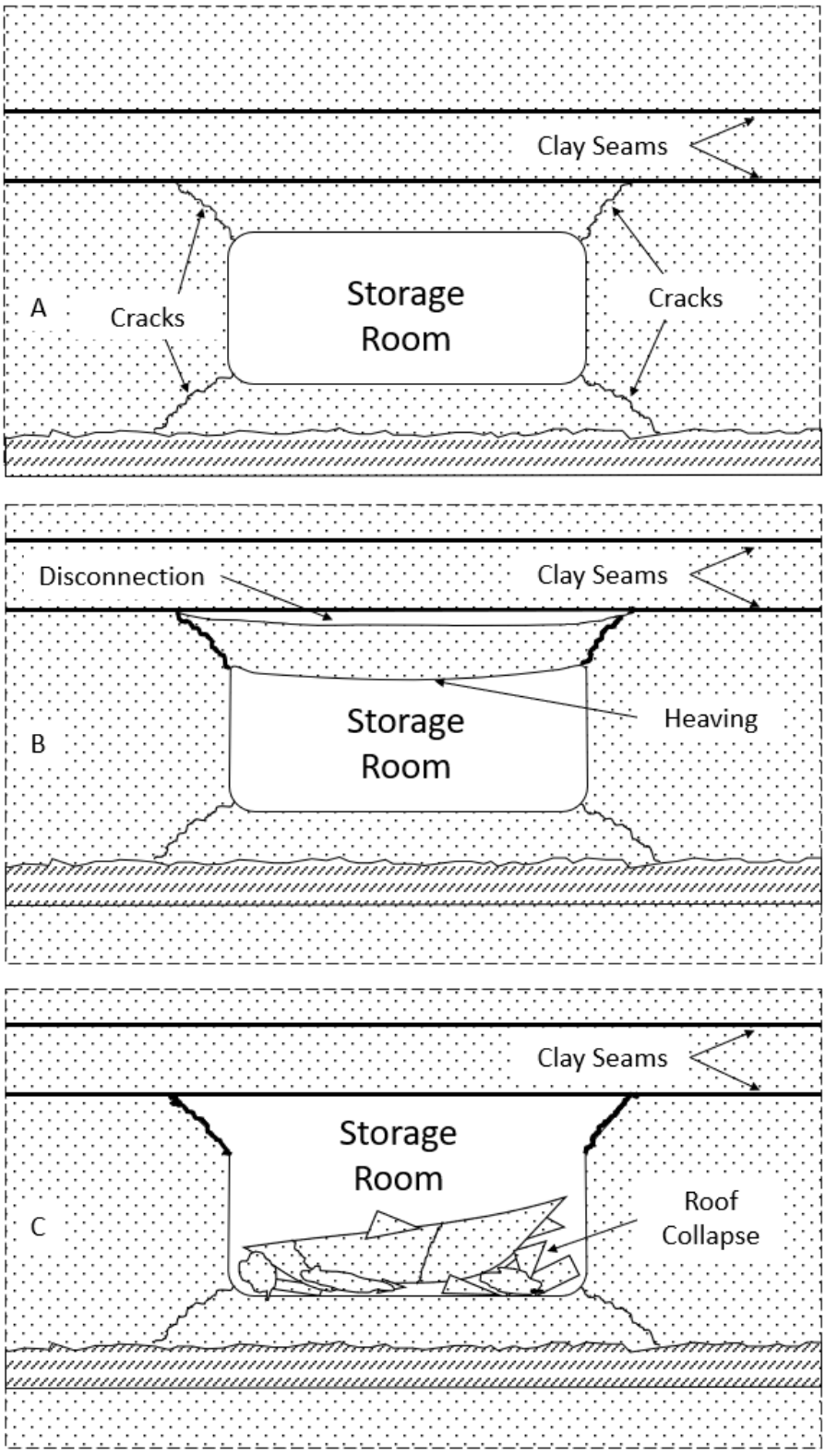

Figure 4: Sequence from corner stress crack propagation to roof collapse.

1.4.3 Why Roof Falls are a Problem

Aside from general safety concerns during waste emplacement if left unmanaged, roof falls also create piles of salt rubble. These piles change transport properties within the repository and can continue to change over time due to the salts creep behavior. Without roof falls, the way in which the transport properties change over time would be different due to the lack of resistance to room closure from rubble, possibly taking longer to creep close, as illustrated in Figure 5. Due to the particularly hazardous properties of the waste contained, it is important to know how fluids may be transported through changing pore structure of the repository. If radioactive material were to be transported out of the repository, impacts on humans and the environment could be detrimental.

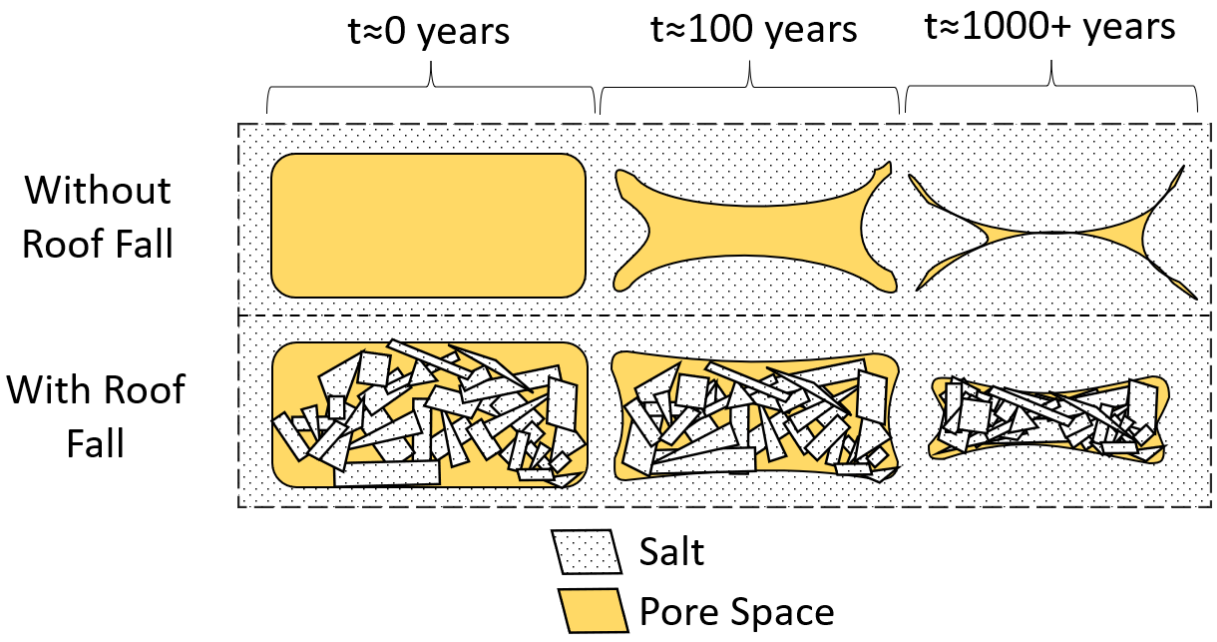

Figure 5: Schematic representation of room closure over time with and without a roof collapse.

Human intrusion scenarios are defined by how the radionuclides contained in the WIPP repository would be transported out of the repository (National Research Council 2001). These scenarios are of particular concern long after the repository emplacement operations have ceased and there are humans who are unaware of the repository's existence. The fact that drilling activities in the region around WIPP are very high suggests that humans in the future may also be incentivized to explore and drill in this area. Drilling through the repository could release radionuclides into the biosphere. The transport properties of the repository dictate whether radionuclides will escape the repository, and at what magnitude. If humans drill through the repository, along with a hypothetical brine pocket beneath the repository as shown in Figure 6, the amount of radionuclides that would be released to the surface depends on the permeability and porosity of the repository. The greater the permeability, the more volume in the repository the brine could flood, and therefore more radionuclides that could be released to the biosphere. Additionally, if the porosity is low with high volumes of brine or gas, larger pressures will build and lead to ease of transport throughout the pore structure of the repository and possibly up a borehole (Reedlunn et al., 2019).

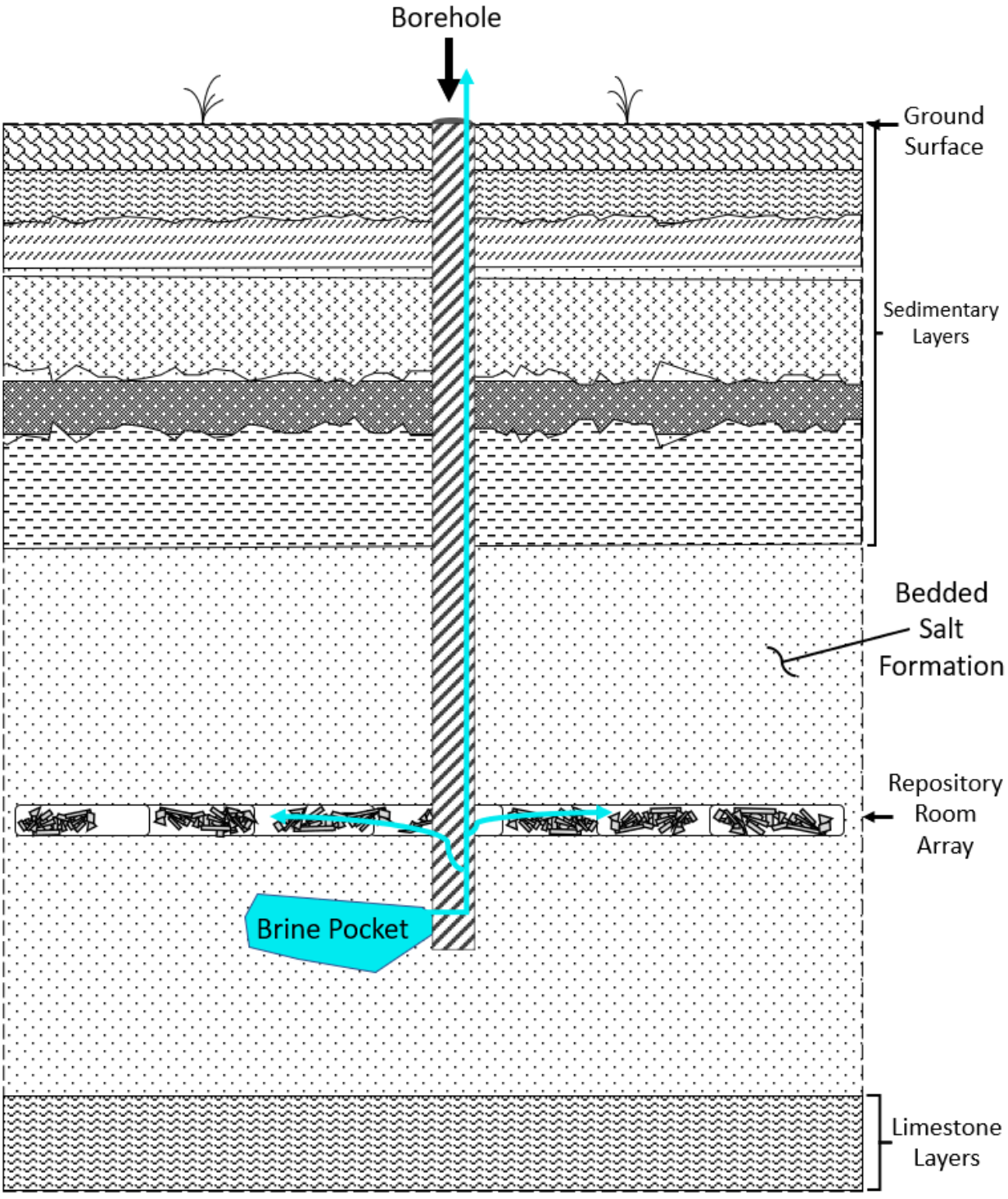

Figure 6: Human intrusion scenario resulting in the hypothetical release of radioactive contaminants into the environment.

1.5 Roof Fall Material Permeability and Porosity

1.5.1 Existing Data on Granular Salt

Roof falls at WIPP alter the permeability and porosity of the repository over time. With the collapse of the roof beam of a room, the beam hits the floor, and breaks up into loose salt rubble pile. This pile of rubble is expected to have a relatively vast grain size distribution with chunks of salt larger than a meter in size and fines smaller than 0.1 mm as observed in the roof fall rubble of SPDV Room 1 in Figure 1 (The Current Bases for Roof Fall Prediction at WIPP and a Preliminary Prediction for SPDV Room 2 1993). While there have been permeability and porosity measurements on granular salt, there have not been measurements on loose granular salt with grain size distributions expected for rubble from roof falls. The majority of measurements have been made on granular salt particles less than about 10 mm and therefore does not cover a grainsize distribution nearly as wide as what is expected from roof fall rubble. Further, most measurements focus on consolidating granular salt at porosities less than about 20% (Brodsky 1994, Cinar et al, 2006, Bechthold and Bollingerfehr 2000, and Ezersky and Goretsky 2014), with only limited measurements on loose salt with greater porosities (e.g., Spangenberg 1998).

1.5.2 Why Not Field Measurements?

Long before rooms are due to collapse, they are decommissioned and shut in as the potential hazards of structural instability increase over time (The Current Bases for Roof Fall Prediction at WIPP and a Preliminary Prediction for SPDV Room 2 1993). To measure the permeability of the roof fall material on site would be hazardous and unreasonable since access to these rooms is purposely made to be difficult.

Limited access to roof fall rubble is also a deterrent to directly sampling the rubble from roof falls to be tested off-site. Additionally, the size and variability of salt grains produced from a roof fall would make accurately sampling the rubble unreasonable. For example, 700 tons of salt rubble was created when the roof of SPDV Room 1 fell in 1991 (The Current Bases for Roof Fall Prediction at WIPP and a Preliminary Prediction for SPDV Room 2 1993). Attempting to sub-sample a representative elementary volume (REV) from a rubble heap such as in SPDV Room 1 would likely require much more effort, machinery, and precautions than is possible.

1.5.3 Predictive Models (K/C)

Predictive models from empirical data for permeability of porous media exist and are based upon different characteristics such as grain shape, grain size distribution, pore volume, saturation, etc. Perhaps the most widely applied predictive model is that developed by Kozeny and Carman in the 1950s known as the Kozeny-Carman formula, which utilizes only the specific surface area and void ratio along with a shape factor to predict the permeability of a porous media (Carrier 2003). This model has been verified experimentally with different types of porous media with varying grain size distributions seen in Chapuis et al. (Chapuis 2012). However, the model has never been employed with grain size distributions of such a wide range as expected from roof fall rubble. For example, the compacted salt samples tested by Brodsky (Brodsky 1994) were fit with the Kozeny-Carman model by Chan et al. (Chan et al., 2001), but the samples' grain sizes did not exceed 10 mm. Since the Kozeny-Carman model has limitations, as any empirical model does, it is not obvious if this model can be used to predict the permeability of the material produced by a roof fall.

1.5.4 Considerations for Laboratory Tests on Rubble

As a result of the limited data on the transport properties of the roof fall rubble, lack of data supporting predictive models with similar characteristics as the rubble, and the difficulties associated with directly testing the rubble on site, laboratory measurements are suggested. There are a number of important considerations when designing a test for measuring permeability and porosity of rubble in the laboratory.

1. Due to limitations in field sampling from actual roof fall rubble, the material for the laboratory testing should, to the extent practical, include a wide range of particle sizes that approximates the rubble.
2. The laboratory testing configuration for permeability and porosity of the artificial rubble should be large enough to contain grain sizes as large as practical while maintaining a representative grain size distribution sample.
3. The testing configuration size is limited because the intent is that the laboratory sample will be placed into a large, but finite sized, computed tomography (CT) scanner. The scanner is intended to be used to map the pore structure and help calculate surface porosity of salt samples to be used in numerical simulations for further analysis.
4. In addition to the size restriction, the sample and testing configuration should be free of metallic objects since they distort and affect CT scans.
5. The measurements should be made with inert gas with respect to salt due to water-based fluids dissolving the salt and altering the sample.
6. Positive pressure would require a confining pressure on the sample to prevent wall flow which can confound permeability measurements. Rubble is particularly difficult in this

regard as the wide range of angular particles tend to produce very rough interfaces with the outer boundary proving sealing difficulties. Vacuum pressure will allow for highly deformable material such as plastic to be used to confine the sample. The material will then compress onto the particles and mold to the edges of the grains, thereby reducing more permeable edge gaps created at the confining walls of the test configuration.

1.6 Objectives

The goal of this study is to simulate material produced by roof falls by including salt particles as large as practical in a loose granular salt mixture and measure the permeability and porosity of the mixture. To achieve this goal, the following objectives must be met:

1. Create an experimental system to measure the permeability and porosity of simulated roof fall rubble. The system will be large enough to fit the large rubble particles, small enough to fit in a CT scanner, contain no metal (or have removable metal parts), and use vacuum pressure to induce flow of gas through the sample.
2. Obtain, prepare, and characterize salt particles to create samples simulating rubble produced by roof falls at WIPP.
3. Conduct, interpret, and analyze permeability and porosity measurements.

2. MATERIALS AND METHODS

2.1 Summary

Laboratory measurements described in this section were conducted on different grain size distributions of loose granular salt mixtures from the WIPP Salado Formation. The gas permeability and porosity of samples of the granular salt mixtures were measured in a large, sealed, vacuum bagged container. Additional complimentary vacuum gas permeability measurements in smaller testing containers were also made. A description of conditions for all tests are given in this section.

2.2 Salt Used to Create Samples

Salt used in this study was collected with two different methods. The first method is simply collecting the salt produced by the continuous miner machine used to mine the WIPP facility's repository rooms (WIPP Site n.d.). This salt is known as Run-of-Mine (ROM) salt and contains grain sizes typically less than 2.5 cm in size as shown in Figure 7. Approximately 18 kg of this ROM salt was provided to the UNM laboratory in buckets in addition to the 160 kg already available at the UNM laboratory. The second method for collecting the salt was by coring. 30 cm diameter salt cores were sampled from the in-situ rock salt formation at WIPP, shown in Figure 8. These large cores were used to produce larger salt grain sizes to simulate grain size distributions found in roof fall rubble. Five of these 30 cm diameter, approximately 0.75-meter in length, solid salt cores were sealed intact in thick cylindrical cardboard cases and transported to UNM tied down in a truck bed. Both ROM salt and salt cores are heterogeneous mixtures of halite, polyhalite, clays, and other minerals (Stormont 1990).



Figure 7: ROM salt upon arrival at UNM in bottom of 60 cm diameter barrel.



Figure 8: Intact 30-cm -diameter solid rock salt core

While ROM salt is already assumed to be in a state similar to the smaller grain sizes found in roof fall rubble, the intact cores require further processing in order to more accurately represent roof fall rubble. The cores broken by dropping them onto a steel plate from a height of approximately 2 meters, producing a wide range of particle sizes. Some of the larger pieces were further broken apart with a hammer. A plastic sheeting was placed around the area to easily gather all the salt pieces produced from dropping the cores. While conditions in a WIPP facility roof fall scenario are not the same, dropping the salt cores to break them up into smaller, jagged, rubble-like pieces was meant to simulate the same type of way salt grains would break apart upon falling from the roof to the floor of a room in WIPP. The main details of a WIPP roof fall,

which deviate from the simulated salt dropping at the lab, are that the roof fall pieces at WIPP would likely include pieces much larger than the cores. The roof fall material would also fall the entire 4.6-meter height of the rooms to the floor and strike the solid rock salt floor below to break apart rather than the steel plate as used in the laboratory.

2.3 Grain Size Distributions

2.3.1 Processing the Rubble Material

Following the dropping/breaking of the salt cores, particles and chunks of salt were collected and classified. Since most of the weight of the salt cores ended up as grains larger than 38 mm and therefore incapable of fitting into a standard sieve analysis (ASTM E11), an arbitrary grain size distribution was used to categorize and quantify these large pieces. The following salt particle sizes are measured based on their largest dimension since most particles had varying dimension ratios and angularity. The five categories to classify this salt are nominal grain sizes 40 cm to 25 cm, 25 cm to 15 cm, 15 cm to 8 cm, 8 cm to 2 cm, and grains smaller than 2 cm. The grains smaller than 2 cm were added to the ROM grain size distribution since they could fit through a standard sieve analysis along with all the other grains in the ROM. As a result, two different grain size distributions were identified as the first being grains capable of fitting a standard sieve analysis called “ROM” and the second being grains too large to fit a standard sieve analysis called “Rubble”.

2.3.2 Processing the ROM Material

Since the standard sieve analysis can only contain a very small percentage of the total ROM available, the ROM salt was sub-sampled to develop its grain size distribution. The ROM was sub-sampled by ‘coning and quartering’, a method involving making a pile of the grains in a cone shape, flattening it into a cake, dividing it into two quarters, and using the two quarters opposite of each other as a sub-sample. This method was repeated until the sub-sample is small enough to fit in a standard sieve analysis.



Figure 9: Quartering the flattened cone of ROM salt in the coning and quartering sub-sampling method.

2.3.3 Rubble and ROM Grain Size Distributions

ROM and rubble materials are stored as separate materials so that they can be mixed to provide desired sample grain size distributions. In addition, the rubble tends to break apart somewhat with handling, so keeping the material separate allows the grain size distributions for rubble to be modified and updated over time. The grain size distributions for the ROM and rubble materials are given in Figure 10 and reveal that the rubble grain size distribution is slightly more than an order of magnitude larger in particle sizes.

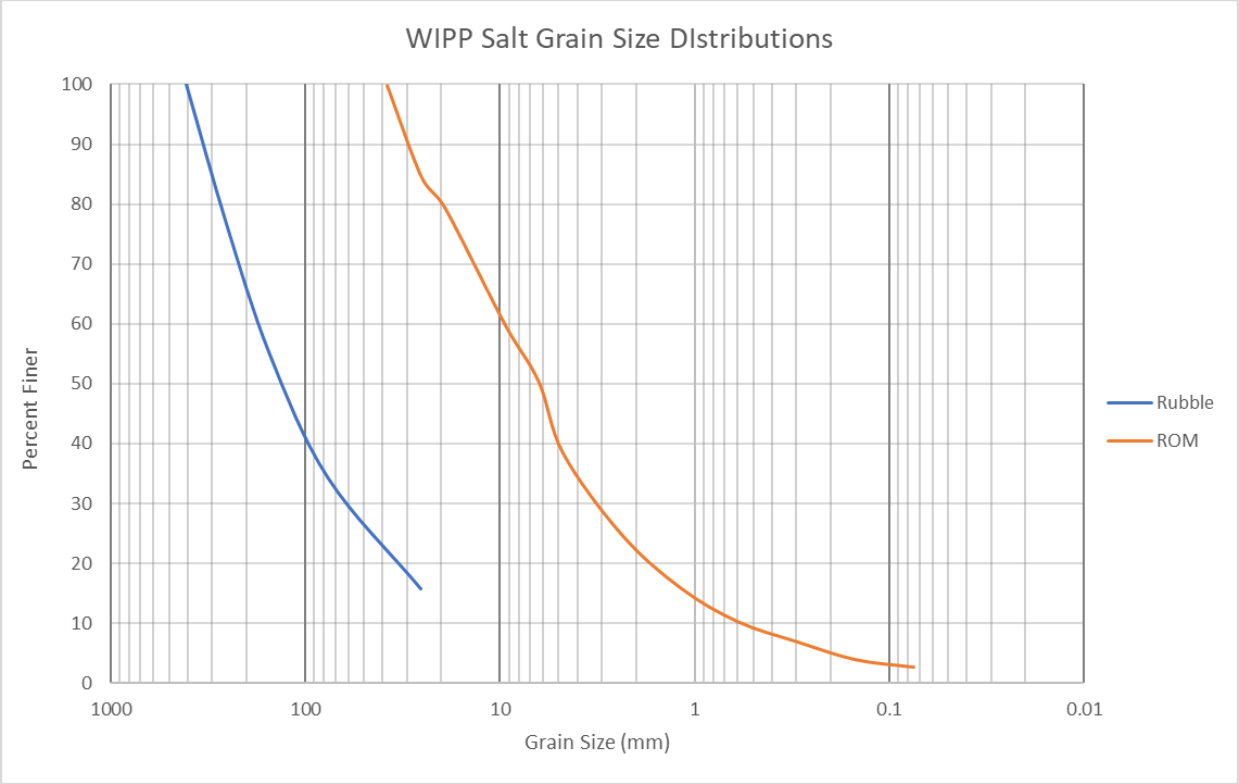

Figure 10: Comparison of the grain size distributions for ROM and rubble salt.

The salt grain sizes used in these experiments cover a wide range of particle sizes, relative to other studies on granular salt, and includes grain sizes of salt much larger. For example, Spangenberg et al. (1998) tested loose granular salt with grains up to 2 mm in size, compared to this study which includes grain sizes up to 400 mm. While roof fall rubble is expected to contain salt pieces over 500 mm in size, the size of the experimental configuration limits the size of particles that can be included to make accurate flow measurements.

2.4 Large-Scale Permeameter/Porosimeter

2.4.1 Experimental Configuration

The experimental configuration shown in Figure 11 below is referred to as the permeameter but is capable of measuring both permeability and porosity of the granular salt. This permeameter has been through numerous modifications to refine measurements and better contain salt samples.

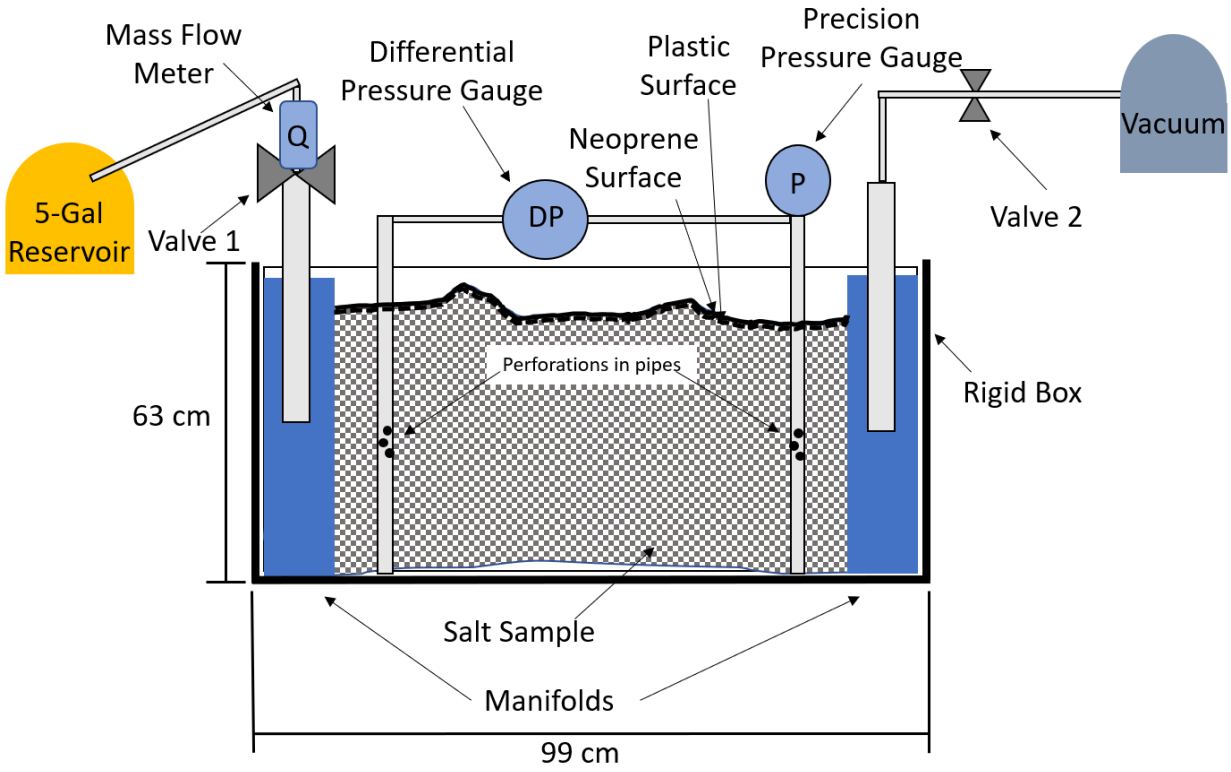

Figure 11: Permeameter schematic cross section.

Excluding the salt sample, the permeameter includes eight main components: rigid box, plastic and neoprene sheeting, manifolds, vacuum source, known volume reservoir, flow measurement components, pressure measurements components, and tubing/piping. These components are shown in Figures 12 and 13 below and are subsequently described in detail.

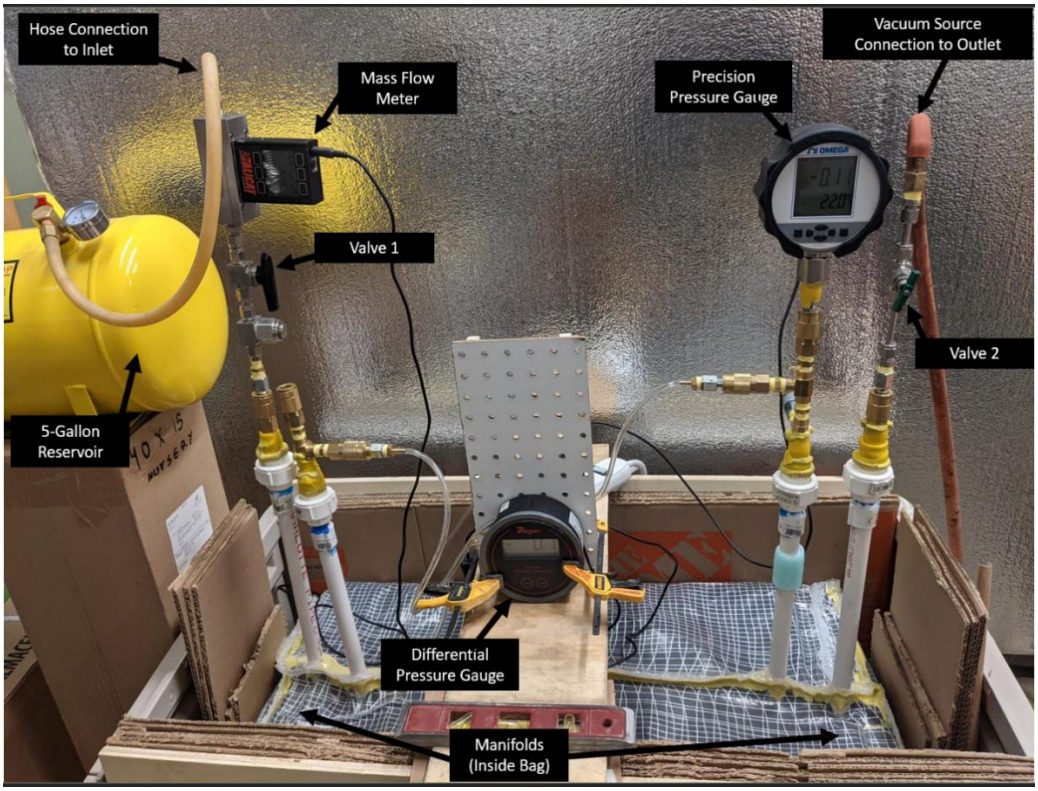

Figure 12: Photo of permeameter with all components and measurement devices attached and ready for measurements.

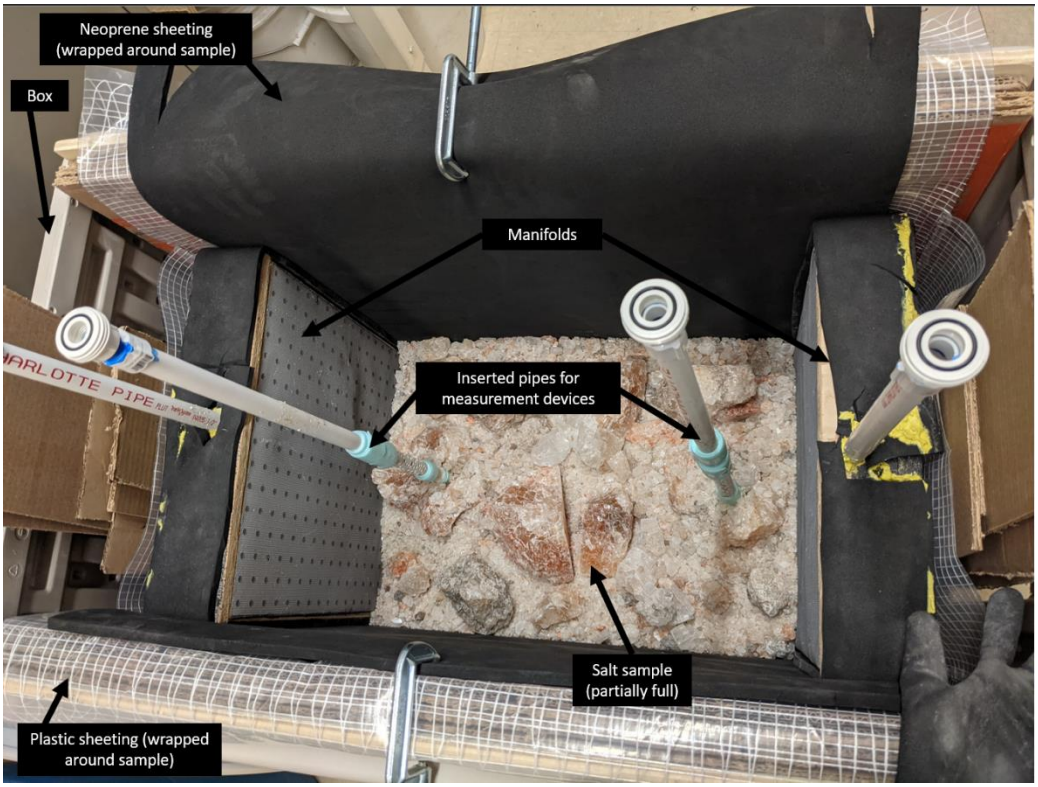

Figure 13: Top view photo of partially filled permeameter without measurement devices attached.

2.4.2 Rigid Box

A rigid plastic box provides the structure for the permeameter as shown in Figure 13. The rigid container must be capable of supporting and retaining the shape of large weights since salt samples weighed more than 200 kg. Deck/patio boxes were used for this application since they are relatively sturdy and built to store large and/or heavy equipment, tools, etc. The deck boxes were also favorable since they contained little if any metal parts as this is essential for CT scanning. The only metal included in the assembly of the deck boxes were screws which were substituted with nylon screws. Additionally, plastic support straps were tied around the boxes for

extra structural strength of the box. Finally, the deck boxes were made mobile by placing them on furniture dollies. Since the dolly wheels contained metal, a screwless wooden pallet was placed between the deck box and the dolly so that a pallet jack would be able to place the sample into the CT scanner without the furniture dolly.

The rigid box component was modified by removing the lid to access the entire top of the sample. Also, non-structural pieces from the four sides containing the sample were removed to give some access to the sides of the sample. The dimensions of the box were also modified in July 2021 so that the sample could fit in the CT scanner at Sandia National Laboratories (SNL). Initially, boxes were 120 cm long, 56 cm tall, and 56 cm wide. With the CT scanner constraining the maximum dimension of the box to 100 cm, new boxes with dimensions 99 cm in length, 63 cm in height and 57 cm in width were obtained, modified in the same ways described above, and used.

The final pieces of the rigid box component are the cardboard and plywood placed between the deck box and the plastic that can be seen in Figure 13 surrounding the sample. The plywood and cardboard serve two different purposes. First, to constrain the sample size to a specific dimension so the volume and dimensions of the salt sample can easily be measured. An additional CT scanner constraint of keeping the maximum sample dimension to 61 cm was easily satisfied by inserting cardboard on either side of the box. The second purpose is to add space between the deck box and the plastic to increase access through the holes in the sides of the deck box. During testing, the plastic will hold the salt in place for the box since it is under vacuum pressure and the plywood and cardboard pieces can be removed so that the sides of the plastic can be accessed for repair after the sample is fully constructed.

2.4.3 Plastic and Neoprene Sheeting

Plastic and neoprene sheeting is used inside the rigid box configuration to contain the salt sample and flow gas through it. Numerous types of plastic sheeting were experimented with to refine the testing configuration and meet the following requirements:

1. The plastic needed to be impermeable to isolate flow through the sample. Many locally sourced plastic sheets used as moisture barriers or for construction site cleanliness were used but found to have visible manufacturing flaws including small holes and tears (i.e., permeable). Hence, they were not suitable for use.
2. Plastic with strength and rigidity to avoid punctures by the rough edges of salt grains, but deformable enough to contact all the salt grains on the sides of the sample to reduce macropores and avoid the wall effect. Initially, plastics tested were linear low-density polyethylene (LLDPE), low density polyethylene (LDPE), and polyethylene (PE) from 4 to 10 mil thick. These plastics proved to typically break under vacuum at the ridged and pointed surfaces of the salt grains.
3. Plastic that can easily be sealed following reasoning in the first requirement. Many methods were attempted to seal the plastic bag so that air would not leak into the sample during testing. Methods include heat welding of the thermoplastic PE, vacuum tape, and special PE glue. A combination of polyethylene glue and vacuum tape was found to provide the best seal of the plastic.

The plastic found to best meet these requirements was a 10-mil thick coextruded film consisting of two layers of LLDPE with a reinforcing nylon thread grid between them. This plastic sheeting was used for most of the tests coupled with a 9.5 mm thick neoprene sheet as

shown in Figure 13 (above). The neoprene sheet aided the plastic to meet the second requirement. Since the neoprene is very deformable, impermeable, and puncture resistant, it works well to protect the plastic sheeting from pointed or rough salt grain edges while molding to the shape of the salt and filling-in macropores along the surface of the sample. The initial alternative to this neoprene sheeting was a thinner, approximately 2 mm thick dish packing foam. This foam proved to be sufficiently strong and was used for smaller grained material (ROM) testing. However, the thin foam tore when used with the larger salt grains found in the rubble and was substituted for the thicker neoprene sheeting.

2.4.4 Manifolds

The manifolds shown in the Figures above serve to disperse gas flow over the entire cross-sectional area of the sample to create one-dimensional flow in the horizontal direction. The manifolds are hollow, rigid, and made of wood pieces glued together. A wooden perforated pegboard is used on the side of the manifolds in contact with the salt sample to distribute flow across the area of the sample. Fiberglass screens are also used on this side of the manifold to prevent smaller salt grains from falling through the pegboard holes and into the manifolds' open space. Manifolds were originally designed to have gas flow enter through a PVC pipe attached to each manifold's face opposite of the salt sample. This however, proved to make the sealing of the plastic bag very difficult at the point the pipe entered the plastic bag. Instead, a PVC pipe was inserted through a drilled hole on the top of the manifolds at the center where the final seal is made along the top of the plastic bag as shown above in Figure 13.

2.4.5 Vacuum Source

The vacuum source is connected to one of the manifolds and defines the outlet through the sample. Three different vacuum sources were used including an industrial Shop-vac, the laboratory supply vacuum, and an electric portable vacuum. The industrial Shop-vac did not supply a steady flowrate, so the lab vacuum was used for most tests solely because the electric vacuum was more difficult to connect to the piping.

2.4.6 Reservoir

A gas tank with a known volume of 18.92 L was used as a reservoir to make porosity measurements via the gas expansion method further explained later in this section. In this method, knowing the exact volume of the reservoir is necessary.

2.4.7 Flow Measurements

Flow is measured and recorded at the inlet of the sample before entering the inlet manifold as shown in Figure 12. Flowrate was initially measured using rotameters to provide a volumetric flowrate. This measurement was then converted to a standard flowrate of air by measuring the gas pressure. Since the rotameters had limited accuracy and resolution, an electronic mass flowmeter was used instead for most tests. This flowmeter (Alicat model M-100SLPM) measures pressure and temperature to calculate and display a standard flowrate in the range of 0 to 100 standard liters per minute (SLPM). The flowmeter's resolution of 0.1 SLPM also outperformed any of the rotameters. Finally, a 150-micron filter was placed in between the

sample inlet and the mass flowmeter to prevent any backflow of small salt particles into the mass flowmeter, which would potentially damage the device.

2.4.8 Pressure Measurements

Pressure measurements are made at different locations on the sample to calculate the pressure gradient across the salt sample. Initially, pressure gauges were attached with the same lines connecting the sample to the inlet/atmosphere and the outlet/vacuum source. This configuration measured the dynamic pressure since these pipes had gas flowing through them and past the gauges; therefore, a new system with perforated PVC pipes inserted directly into the salt was adopted as shown above in Figure 12. This configuration allowed for measurements at static pressure well-like points in the sample and did not include pressure losses due to in-line plumbing.

The first pressure gauges used to measure the pressure gradient in the salt sample were vacuum gauges with resolutions of approximately 50 Pa. Other vacuum gauges with slightly higher resolution were acquired to improve measurements. Finally, high-precision gauges from Omega Engineering were purchased (Omega model DPG210). These precision gauges record in the range of -100 kPa to 100 kPa and have resolution of approximately 10 Pa.

To further refine measurements, differential pressure readings were implemented. A precision differential pressure gauge from Dwyer (Dwyer model DM-2002-LCD) was attached by hoses to the static pressure head inserted PVC pipes. Since the absolute pressure in the sample is required for permeability measurements, one precision Omega gauge was also attached to one of the same pipes. The differential pressure gauge improved pressure measurement resolution to

0.1 Pa and has a range of 0-100 Pa of differential pressure. Additionally, a lab-made differential water manometer was used with a microscopic camera to attempt to further improve differential pressure reading resolution. However, this method could not provide differential pressure resolution below 10 Pa and was replaced with the Dwyer differential pressure gauge.

2.4.9 Tubing/Piping

The tubing and piping of the permeameter is designed for easy removal of any metal parts, including measurement devices, without disturbing the sample. The plumbing is also designed to easily make permeability and porosity measurements of the salt sample without disturbance. PVC pipes of 1.2 cm diameter are used to transport flow through the plastic bag and into the tops of the manifolds at the inlet and outlet. These pipes are also inserted into the salt sample where pressure readings are made. The tops of all these pipes are fitted with a PVC union which utilizes a rubber O-ring and allows for quick connection/disconnection of items in-line above. Above each PVC union are 6.4 mm diameter brass quick-connects which are self-sealing when their body disconnects from the stem. These quick connects allow for measurement devices to be connected, removed, or relocated in the permeameter easily without disturbing the sample. Each measurement device was attached to a quick-connect stem. The reservoir and vacuum source require an additional flexible vacuum hose to attach to these quick-connect stems.

2.4.10 Experimental Procedure for Measuring Permeability

To measure the permeability of a salt sample, all components of the permeameter are necessary except for the reservoir. First, the valve between the flowmeter and the inlet is opened

to expose this end of the sample to the atmosphere. Once the vacuum source is turned on and the needle valve between the source and the piping is opened, the bag will collapse onto the salt due to the vacuum inside the bag. Then, air will flow through the flowmeter at the inlet, through the salt sample, and finally toward the vacuum source. Pressure and flow measurements are made at steady-state flow, so time is allowed for the flowrate and pressure to stabilize. Once steady-state flow has been reached, measurements of pressure in the bag, differential pressure across the sample, and flowrate through the sample are made. This set of measurements is repeated for at least 5 different steady state flowrates using the needle valve to regulate flow. The repetition of these measurements at different flowrates is used to correct permeability measurements for non-linear flow. This correction is explained in further detail later in this section.

2.4.11 Experimental Procedure for Measuring Porosity

The following experimental method described for measuring the porosity of a given salt sample is referred to as the "gas expansion" method. This method requires the reservoir to be connected to the system at the inlet. The differential pressure gauge is also removed from the system using the brass quick connects. With the entire system at atmospheric pressure, the reservoir is isolated from the sample by closing the valve connecting it at the inlet. The sample is then pressurized with the vacuum source to some sub-atmospheric pressure, and isolated from the vacuum source. Once the pressure in the bag has stabilized, the valve at the inlet is opened to expose the reservoir at atmospheric pressure to the pressurized sample, causing gas to flow from the reservoir into the sample. The pressure is monitored with time. Typically, the pressure rapidly increases but most tests did not fully stabilize at an equilibrium pressure. Instead, a very slow and nearly constant pressure change was detected which was attributed to very small leaks

in the sample. This system leakage rate can be quantified and subtracted from the measured pressure equalization.

2.5 Permeability and Porosity Interpretation

2.5.1 Permeability Interpretation

In interpreting the permeability of salt samples, Darcy's law for porous media is used. For one-dimensional, steady-state, isothermal flow of an ideal gas, the following form of Darcy's law is used to calculate the permeability:

$$\frac{{P_u}^2 - {P_d}^2}{L} = \frac{\mu Q}{kA} \tag{1}$$

Where:

- P_u is the pressure measured upstream in the sample (atmosphere/flowmeter side).
- P_d is the pressure measured downstream in the sample (vacuum side).
- L is the length of the porous media between the upstream and downstream pressure measurements.
- μ is the dynamic viscosity of the gas. For air at $20℃$, μ is equal to approximately 1.76×10^{-5} Pa·s.
- Q is the standard flowrate through the porous media.
- k is the permeability.
- A is the cross-sectional area of the sample.

The length (L) and the cross-sectional area (A) are measured with a tape measure prior to permeability tests. Then, the mass flowrate (Q) is read directly from the Alicat mass flowmeter at steady state. The absolute pressure downstream (P_d) is calculated by subtracting the measured vacuum pressure, shown by the Omega pressure gauge, from atmospheric pressure. The absolute pressure upstream (P_u) is then calculated by adding the differential pressure, measured by the Dwyer differential pressure gauge, to the absolute pressure downstream (P_d).

With large flowrates through the porous media sample, inertial flow can cause measurements to deviate from the linear Darcy's law. To account for this, an additional term must be added to Equation 1 to correct for this inertial flow component. This equation, often referred to as Forccheimer's equation, is used to describe flow with an inertial or non-linear component (Zeng and Grigg 2006):

$$\frac{{P_u}^2 - {P_d}^2}{L} = \frac{\mu Q}{kA} + \frac{\beta \rho Q^2}{A^2} \tag{2}$$

Where:

- β is the inertial coefficient.
- ρ is the gas density.

This equation can be re-arranged to take on the form: $y = \left(\frac{1}{k}\right) + x\beta$. Pairs of x and y calculated from the measured values at different steady-state flowrates can be used to generate a non-linear flow correction line with a slope equal to the inertial coefficient β, and a y-intercept equal to the inverse of the permeability. In linear flow, the slope of this line becomes zero, corresponding to an inertial coefficient value of zero, and resulting in Equation 2 reducing to

Equation 1. All measurements made on the various salt samples have displayed non-linear flow and have been corrected using this method.

Another important characteristic of flow through porous media which can result in non-Darcy flow is referred to as Klinkenberg effect or gas slippage (Ziarani and Aguilera 2011). This pressure-dependent effect is most prevalent in relatively tight pores in porous media. The magnitude at which this mechanism causes flow to deviate from Darcy's law is estimated from the Knudsen number:

$$Kn = \frac{\lambda}{r} \tag{3}$$

Where:

- Kn is equal to the Knudsen number.
- λ is equal to the molecular mean free path of gas.
- r is equal to the pore radius.

Gas slippage occurs with Knudsen numbers greater than 0.01 (Ziarani and Aguilera 2011). Since the maximum Knudsen number for the porous media in our samples was calculated to be less than 0.001 with an assumed pore radius of 0.2 cm, gas slippage effects were ignored in all permeability interpretations.

2.5.2 Porosity Interpretation

Porosity measurements are made using the gas expansion method. Interpretation of the data collected is derived from Boyle's law:

$$P_1V_1 + P_2V_2 = P_3V_3 \quad (4)$$

Where P_n and V_n are measured pressures pertaining to their corresponding volumes. The measurements made in the gas expansion experiment are as follows: P_1 is the atmospheric pressure at which the volume of the reservoir (V_1) is contained. P_2 is the sub-atmospheric pressure at which the volume of the sample space (V_2) is contained. Once the valve between the two volumes is opened allowing the pressures to equalize, P_3 is the equalized pressure contained by the combined volumes, V_1 and V_2, which is equal to V_3. Since V_1 is the known volume of the reservoir, and all the pressures are measured, substituting V_3 with $V_1 + V_2$ leaves V_2 as the only unknown. Equation 4 can then be rearranged to solve for V_2 in the following expression:

$$V_2 = \frac{V_1(P_1 - P_3)}{P_3 - P_2} \quad (5)$$

By measuring the volumes of the manifolds and piping associated with V_2, the volume of voids in the sample can be calculated with the equation:

$$V_{voids} = V_2 - (V_{plumbing} + V_{manifolds}) \quad (6)$$

Finally, the porosity can be calculated with an estimated measured volume of the space which the sample occupies in the equation:

$$\varphi = \frac{V_{voids}}{V_{sample\ space}} \quad (7)$$

Additionally, since the weight of the salt in each sample is measured, the weight can be divided by the density of the salt to calculate the volume of salt inside each sample. The void volume can then be estimated by subtracting this volume of salt from the measured sample space

volume. Since both this "weight/density" method of calculating porosity and the gas expansion method use the estimated $V_{sample\ space}$ measurement in their calculations of porosity, they are combined by averaging the calculated sample volumes to better estimate the sample space volume and therefore make a refined porosity calculation.

2.6 Small-Scale Verification Tests

In addition to the permeability measurements made in the permeameter, permeability measurements on the ROM salt grain size distribution were also made in what is referred to in this section as the "Small-Scale Permeameter".

2.6.1 Reasoning for Verification Tests

The small-scale permeability measurements of ROM salt were made to verify the ROM permeability results from the box permeameter. There were uncertainties as to if the flow through the permeameter was truly one-dimensional throughout the cross section of the sample. If the plastic bag containing the salt sample had creases letting significant amounts of flow to bypass the porous media, permeability measurements made in the permeameter would be inaccurate. Inaccuracy of permeability measurements could also be caused by the manifolds not distributing the flow of gas well along the cross-sectional area of the salt sample. The elimination of the manifolds and introduction of wall containment with dish-pack padding were used to reduce these uncertainties by obtaining and comparing permeability measurements of ROM salt from the permeameter and small-scale permeameter configurations.

2.6.2 General Experimental Configuration

The experimental configuration and corresponding schematic are shown in the Figures below.

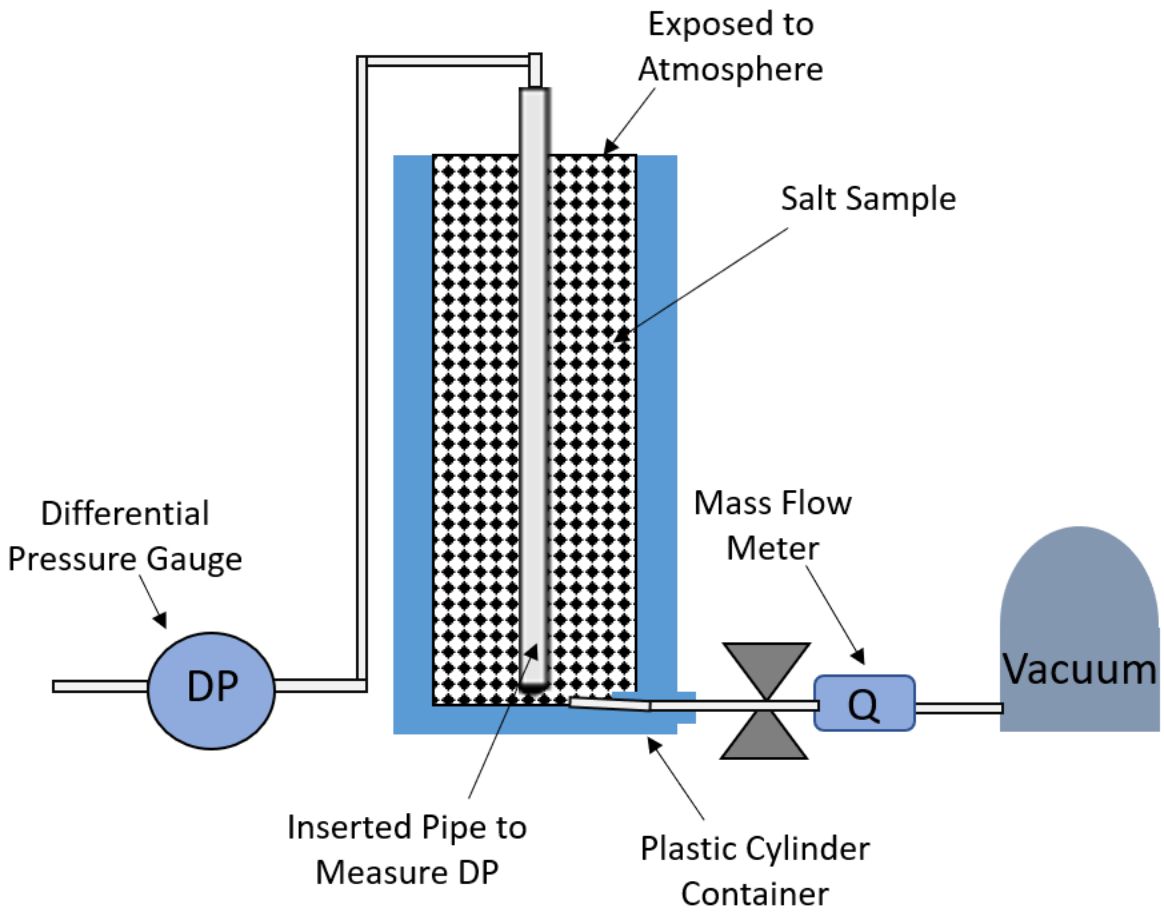

Figure 14: Small-Scale Permeameter schematic.

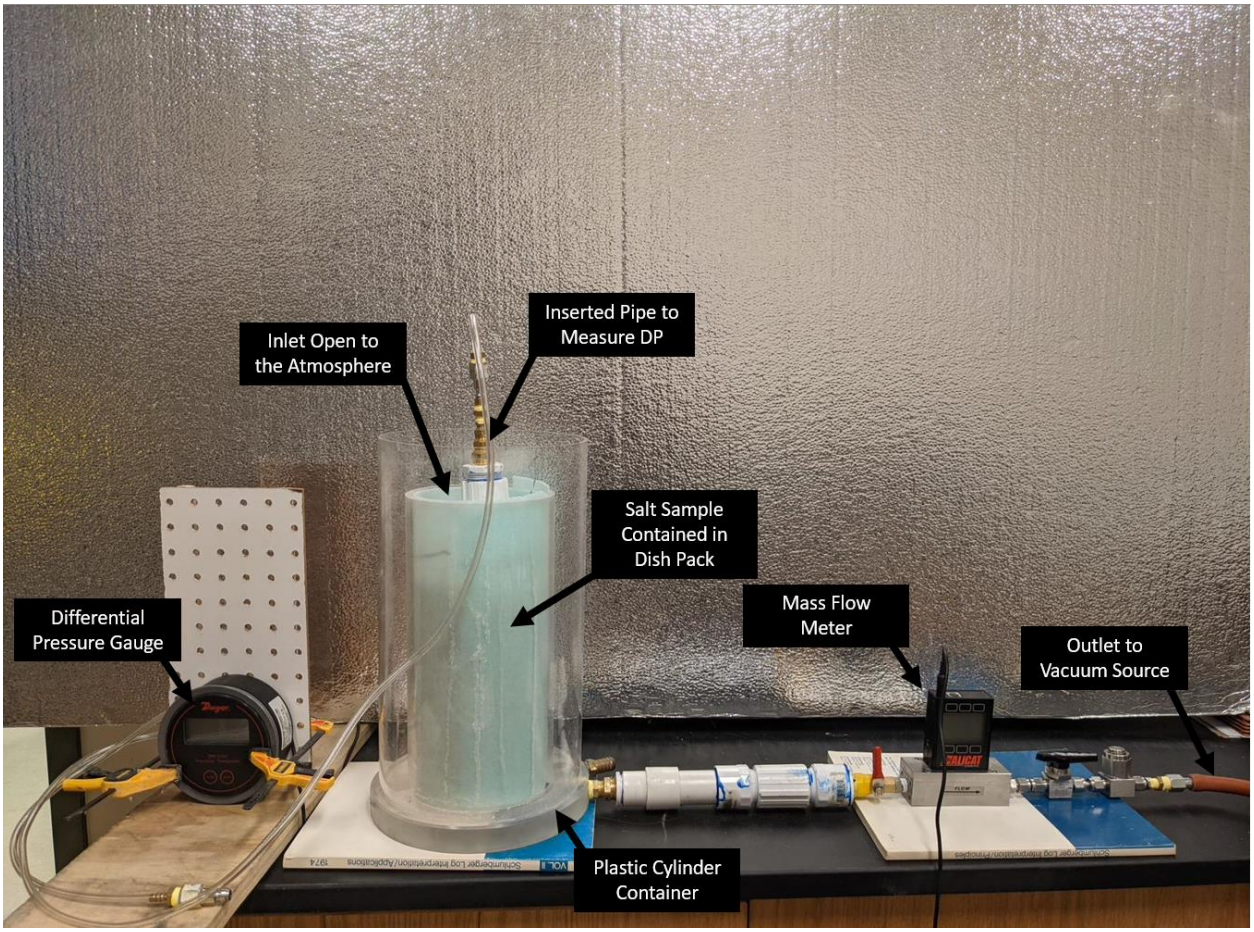

Figure 15: Photo of the Small-Scale Permeameter with all measurement deviced attached.

In this configuration, the differential pressure gauge measures the pressure at the bottom of the salt sample since the other end of the differential pressure gauge is open to the atmosphere. This is because the inlet or top of the salt sample is also open to the atmosphere. With this configuration, the Omega pressure gauge is not necessary.

2.7 Resolution of Measurements

The range and resolution of the measurement devices used in the experiments dictate what range of permeabilities can be measured. For each configuration, the resolution of the differential pressure measurement limits the maximum permeability that can be measured. Although larger flowrates can be used to induce a larger pressure drop, the experiment is also limited by the strength of the sealed plastic bag. Exceeding -20 kPa of pressure in the bag may create a tear and produces an upper limit for how much pressure and flow can be applied on the sample.

Approximately -20 kPa of pressure was applied to the fourth built rubble sample which resulted in a flowrate of 19 SLPM. At this combination of pressure and flowrate, the differential pressure gauge was still unable to resolve a pressure drop across this rubble sample, and displayed a reading that fluctuated between 0 Pa and 0.1 Pa. In order to estimate the maximum measurable permeability, the differential pressure was assumed to be 0.1 Pa. With a pressure drop of 0.1 Pa, pressure in the sample of -20 kPa, and flowrate of 19 SLPM, the calculated maximum measurable permeability is approximately $2.8 \times 10^{-9} m^2$.

2.8 Test Conduct

Sets of permeability and porosity measurements were made on various salt samples of different grain size distributions. However, due to densification, a given salt sample of unique grain size distribution may have multiple different permeability and corresponding porosity measurements at varying levels of densification. Densification of samples allows for different permeability and porosity measurements to be made on a single sample at different levels of

densification. While some densification was intentional, as described in the following section, there may have been some inadvertent densification due to varying effects such as moving samples around the laboratory or applying and removing vacuum pressure to salt samples.

2.8.1 Densification

Densification of samples was achieved with vibration by several different methods. The first method simply used a vibration table. Since samples in the box permeameter exceeded the weight capacity of the vibration table, this method could only be used on samples contained in the small-scale permeameter. The second method involved rolling the box permeameter full of salt on an asphalt pavement. The rough pavement provided a rumble strip effect on the salt sample, helping consolidate it (noted by change in volume level). Different methods, including striking the box repeatedly with a hammer or using a concrete vibrator rod, were used, but proved to be much less effective than rolling the sample around on pavement. The last method used is similar to the third method and is the transport of the permeameter from the laboratory at UNM to the scanning facility at SNL via truck bed. This method had an effect on the sample very similar to the second method.

2.8.2 Samples and Test Conditions

The following section describes the various samples successfully tested along with some key parameters which make them unique. Additional information regarding unsuccessful samples is contained in Appendix A. The configuration the sample was tested in, the amount of ROM or rubble in the grain size distribution, and the 3 methods used for densification are all described along with another important parameter: the leak rate of the sealed bag. Due to

relatively large leak rates, several samples were redone, but their measurements omitted. High leak rates into the sample reduce the accuracy of permeability measurements since the flowrates measured include gas that does not directly flow through the entire length of the sample. The locations of leaks are unknown, so correcting for these leaks accurately is not possible. As leak rates increase and approach induced flowrates measured, permeability measurements become more inaccurate. Since leak testing was done at around 15 kPa of vacuum pressure, the flowrate of leakage into the bag can be calculated and compared to the flowrates measured during permeability testing. Flowrates induced across samples are typically measured in the range of 5-15 SLPM, thus the acceptable leak rates all fell within 3% of the induced flowrates.

Table 1: WIPP Salt Samples Tested and Their Key Parameters

Name Date Constructed	Experimental Configuration	Grain Size Distribution	Vibration Method	Approx. Leak Rate (kPa/s)
ROM 2 5/27/2021	Permeameter (1.2 m box)	100% ROM	Rolling on Pavement	0.0012, (0.140 SLPM)
Small-Scale 1 6/21/2021	Small-Scale Permeameter	100% ROM	Vibration Table	NA
Rubble 3 7/30/2021	Permeameter (1.2 m box)	70% Rubble (Up to 25 cm chunks)	Rolling on Pavement	0.00061, (0.072 SLPM)
ROM 3 8/26/2021	Permeameter (1 m box)	100% ROM	Rolling on Pavement	0.0020, (0.070 SLPM)
Rubble 4 9/16/2021	Permeameter (1 m box)	70% Rubble (Up to 25 cm chunks)	Rolling on Pavement	0.00070, (0.072 SLPM)
Rubble 5 11/5/2021	Permeameter (1m box)	20% Rubble (Up to 25 cm), 80% ROM	Truck Bed Transport	0.00066, (0.054 SLPM)
Rubble 8 1/28/2022	Permeameter (1m box)	40% Rubble (Up to 25 cm), 60% ROM	None	0.0010, (0.093 SLPM)

3. RESULTS AND DISCUSSION

3.1 Permeability vs. Porosity Results

3.1.1 Data Included

The experimental results presented in this study consist of data collected from seven of the twelve salt samples constructed throughout this study. As seen in Figure 16 below, these samples are Rubble 3, 4, 5 and 8, ROM 2 and 3, and Small-Scale 1. The remaining five samples, for which data is not presented, are described in Appendix A along with reasons for omitting.

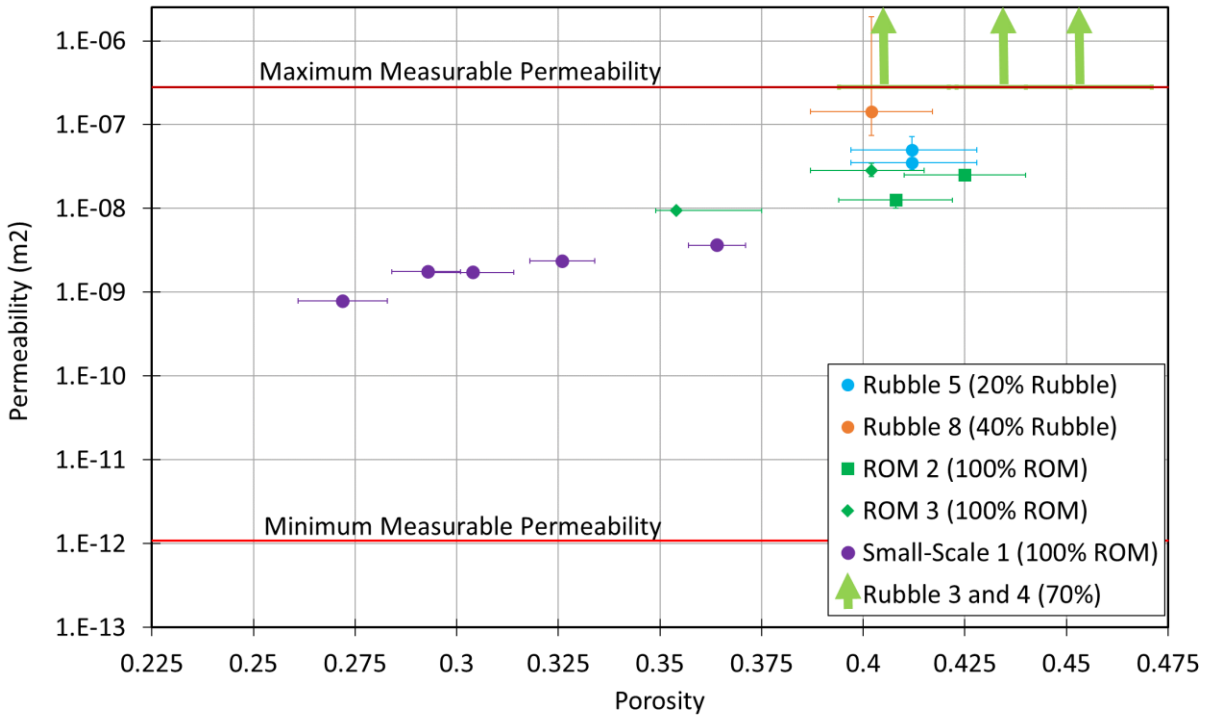

Figure 16: Permeability vs. porosity relationship for seven different samples. ROM 2 and 3, and Rubble 3 and 5 each have two data points, one before densification and one after. Small-Scale 1

has 5 data points: two for one round of filling, then shaking, and three for another round of filling and shaking twice. Rubble 4 and 8 only have one data point.

3.1.2 Error Bars

Error bars for permeability and porosity measurements are given in Figure 16. For the permeability measurements, the error bars were estimated based on the differential pressure measurement as measurements were often made near the 0.1 Pa resolution of the differential pressure gage. The upper and lower bounds of expected error for this measurement were found by adding and subtracting 0.05 Pa from each differential pressure measurement. Since the differential pressure readings become larger and therefore further from the resolution of the differential pressure gauge, the permeability error for lower permeability samples such as ROM samples is low.

For porosity, the error bars were calculated from the dimensional measurements of the sample space which are measured by hand with a tape measure. This measurement has potential error due to the uneven face at the top of the sample where there is no rigid wall or surface to contain and delineate the dimensional measurement. Since the small-scale configuration only has two dimensional measurements (radius and length of sample) and the radial dimension is bounded by the rigid plastic cylinder, the upper and lower bounds of the error associated with porosity measurements are calculated by adding and subtracting 3.175 mm from the cylindrical length. This is the typical size of grains causing discontinuous bumps on the surface of samples. The dimensional measurements of the large-scale permeameter sample space are all less certain since the weight of the sample causes the sides of the rigid box to bend and bow out slightly.

Therefore, the bounds of the error associated with the porosity of samples in the large-scale permeameter are calculated by adding and subtracting 6.35 mm from each of the three dimensions of the sample space since this length is near the measured offset of different areas along the top surface of samples.

3.2 Discussion of Results

3.2.1 ROM Tests Indicate Permeability Increases as Porosity Increases

The data from the ROM samples indicate permeability increases with increasing porosity. This trend is expected since the larger the connected pore space in a sample is, the more permeable it is expected to be. While this trend is very clearly seen in Figure 16 for the small-scale permeameter data, it is less clear for data collected in the large-scale permeameter. This is likely since there is less certainty in the sample space dimensional measurements in the large-scale permeameter. The uncertainty in this trend, associated with data collected in the large-scale permeameter, is accounted for in the larger horizontal error bars.

3.2.2 ROM Samples Have Lower Permeability Than Samples Which Include Rubble

The addition of larger grains of salt into the grain size distribution is expected to increase the permeability of the sample because of the larger pore spaces they create. The measurements revealed that samples containing rubble have larger permeability than that of samples only containing ROM. The sample containing the highest percentage of rubble, Rubble 8, has the largest permeability. Rubble 8 is followed by Rubble 5, which contains less rubble and has a lower measured permeability. However, when compared to samples without any percentage of

rubble, Rubble 5 experiences a greater permeability. Additionally, Rubble samples 1-4 are expected to have the largest permeabilities since they contain 70% Rubble and are outside of the measurable permeability domain.

3.2.3 Difference Between Small and Large-Scale Measurements on ROM

One significant difference between samples in the large and small-scale permeameters is the direction of flow. The difference in flow direction through the sample will result in a difference in measured permeability if the porous media is anisotropic or layered. The reason layering is expected in these mixtures is discussed more in Section 4, but this is a potential reason samples in the large-scale permeameter had a larger permeability for ROM salt than the small-scale permeameter. As smaller particles settle within larger pore spaces due to gravity, vertical flow pathways become more clogged by these smaller particles than horizontal flow pathways as shown in Figure 17 below.

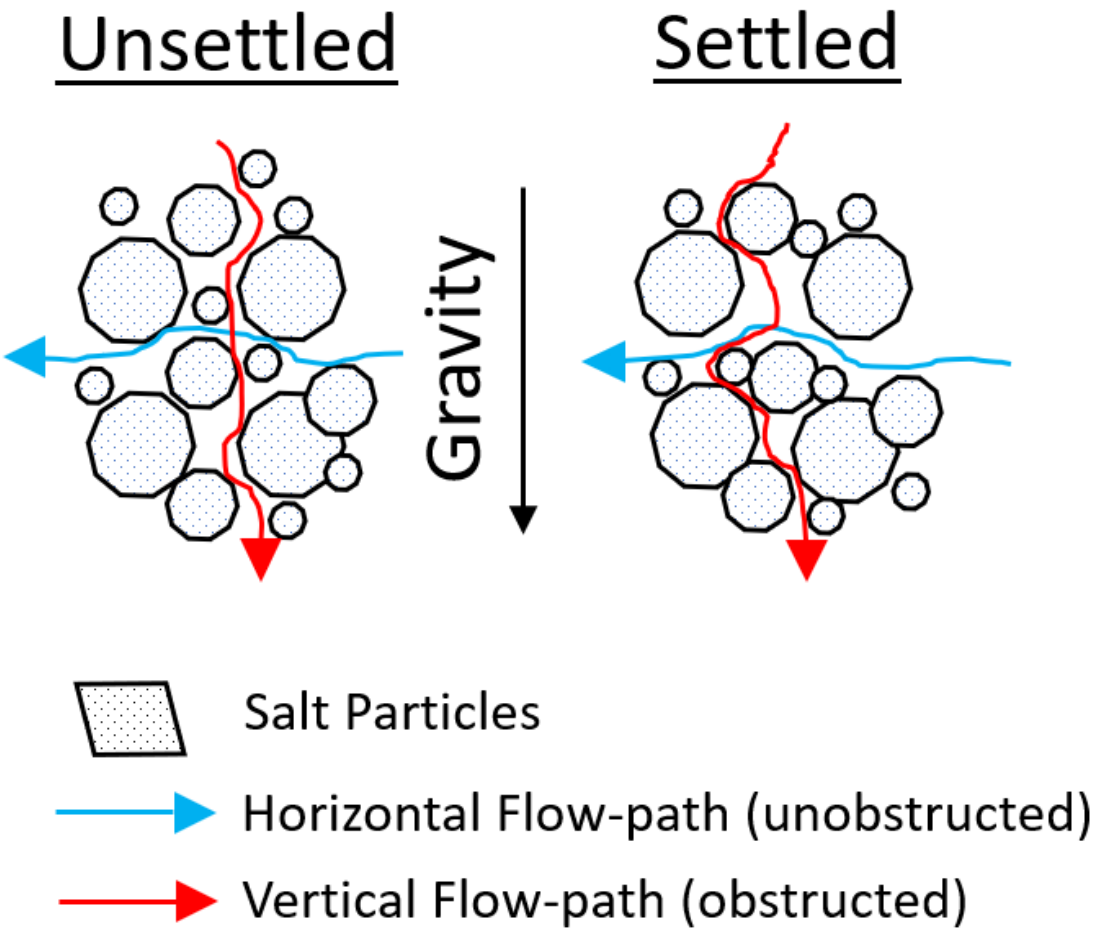

Figure 17: Schematic of layering creating a difference in flow direction pathways.

Another noticeable difference between the small and large-scale results is that the large-scale permeameter measured larger porosity of ROM salt than the small-scale permeameter in nearly every measurement. This result may be due in part to differences in vibration methods. The shake table was able to densify samples in the small-scale permeameter, but the large-scale permeameter exceeds the weight capacity of the shake table and was densified by rolling it on rough pavement. This pavement method was likely less effective in densifying the salt compared to the shake table.

4. ANALYSIS

4.1 Permeability vs. Porosity Relationship with Grain Size Distribution: Kozeny-Carman

The measured permeability and porosity data can be compared to predictions from models of permeability as a function of grain size and/or void characteristics. These models have been developed for porous media with a much narrower grain size range and have been verified most frequently by tests conducted with water under positive pressures. We are interested to determine if these models can be applied to the materials and configuration of the tests presented here.

A widely used and accepted predictive model for the permeability of porous media is a model developed in 1956 called the Kozeny-Carman (KC) equation (Carrier 2003). This model is used to estimate the hydraulic conductivity of a porous media using Equation 8 below.

$$k = \frac{\gamma}{\mu} \cdot \frac{1}{C_{K-C}} \cdot \frac{1}{S_0^2} \cdot \frac{e^3}{1+e} \tag{8}$$

Where:

- k is the hydraulic conductivity.
- γ is the unit weight of the permeant
- μ is the dynamic viscosity of the permeant.
- C_{K-C} is the empirical Kozeny-Carman coefficient.
- S_0 is the specific surface area per unit volume of particles.
- e is the void ratio.

4.1.1 Carrier Interpretation of KC

One challenge of implementing the KC model is the estimation of S_0, the specific surface area, since it is not easily measured for most porous media. The method used in this study to estimate S_0 was developed by Carrier in 2003 (Carrier 2003)). This method uses the principle that for uniform spheres of diameter D, S_0 is equal to 6/D. To account for the non-spherical, angular particles, an empirical shape factor (SF) can be used changing the equation from 6/D to SF/D. Additionally, if the media consists of non-uniform spheres, the effective diameter of can be used. This effective diameter can be calculated using the entire grain size distribution with the following equation:

$$D_{eff} = \frac{100\%}{[\sum \frac{f_i}{D_{ave\ i}}]} \tag{9}$$

Where:

- D_{eff} is the effective diameter.
- f_i is the fraction by weight of particles between two sieve sizes: larger [l] and smaller [s].
- $D_{ave\ i}$ is the average particle size between the two sieve sizes calculated with the expression $D_l^{0.404} \times D_s^{0.595}$.

The standard properties of water can then be input into Equation 8 along with the estimation of the specific surface area to yield the following equation for hydraulic conductivity:

$$k = 1.99 \times 10^4 \cdot \left[\frac{100\%}{\left[\sum \frac{f_i}{D_l^{0.404} \times D_s^{0.595}}\right]}\right]^2 \cdot \left(\frac{1}{SF^2}\right) \cdot \left[\frac{e^3}{1+e}\right] \quad (10)$$

From Equation 10, permeability of a porous media can be calculated from k and predicted for a range of void ratios or porosities just by measuring the grain size distribution and determining an appropriate shape factor. For WIPP salt, a shape factor of 7.4 was selected as recommended for "sharp" particles by Fair and Hatch (1993). For reference, Fair and Hatch recommended shape factors in the range of 6.0 (spherical) to 7.7 (angular). Predictive permeability/porosity curves are then established for each of the grain size distributions as shown in Figure 18 below:

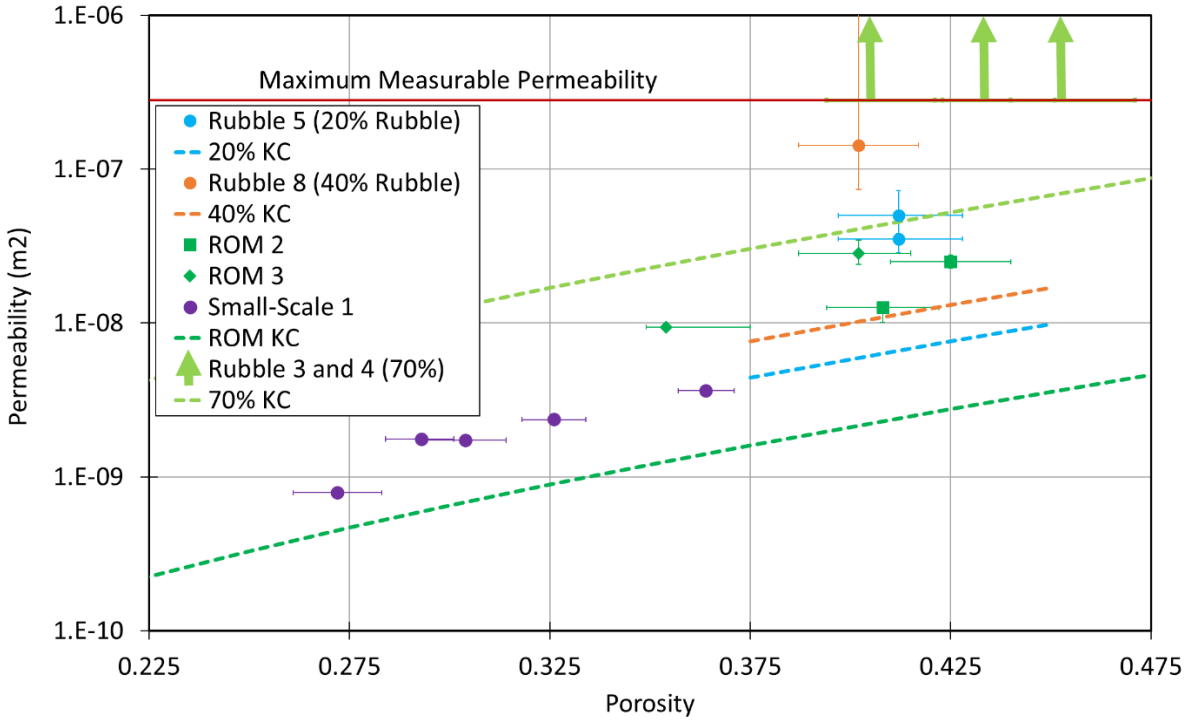

Figure 18: Permeability vs. porosity data with Kozeny-Carman predictive models for each grain size distribution.

4.1.2 Limitations and Suggestions for Improvement

As shown in Figure 18, each of the KC curves under predict permeability with respect to the measurements made for their respective grain size distributions. To understand the reasoning for this trend, the limitations and underlying assumptions of the KC model must be more closely inspected. After all, the KC model itself is built on empirical results of experiments conducted under different conditions than that of the experiments in this study.

A major assumption of the KC model is that the porous media is homogeneous. Homogeneity in the samples tested in this study is not expected due to the relatively large range of particle sizes. Since many pore spaces in the constructed WIPP salt samples are expected to be very large relative to many of the finer salt particles, it is expected that there are not enough smaller particles to fill in these larger voids and create a homogeneous mixture. Since the KC predictive model is weighted very heavily on the finest particles due to their significant effect on the mixture's total specific surface area, it is expected that these finest particles are being overrepresented in the KC prediction since there are not enough of them to fill in the larger pore spaces and create a homogeneous mixture.

Another way in which the samples may deviate from homogeneity is due to settling of the particles causing them to be stratified. Settlement and stratification occur when relatively small particles migrate vertically downward through the larger pore spaces. The finest salt particles are likely to settle to the bottom of the large pore spaces or completely to the bottom of samples as shown in Figure 17. As a result of this layering, the vertical permeability of a mixture will be lower than the horizontal permeability. This effect is well illustrated in Figure 18 by the fact that the 100% ROM mixture permeability measurements collected in the large-scale permeameter (horizontal permeability configuration) are underpredicted much more by the KC model than the measurements made in the small-scale permeameter (vertical permeability configuration).

One parameter of the KC model, which is easily modifiable and directly impacts the two above limitations, is the effect of the finest grain particles in the mixture. Since the KC model uses an estimated specific surface area of the mixture to predict permeability, the fine particles in

the mixture impact the prediction substantially since they have the largest specific surface area to volume ratio. In an isotropic homogeneous mixture, more fines in the mixture would cause the permeability to decrease as the KC model predicts. However, since the fines may not be distributed uniformly in the mixtures used in this study, these fines may be overrepresented in their impacts on the permeability predicted by the KC model. Because the specific surface area in the KC model is calculated by the sum of the weight fraction of particles between different sieves, the KC model can be modified by excluding some of the fines from the model.

The KC model was adjusted to better match the experimental results by removing the finest fractions from the three different grain size distributions (Figure 19). The amount of fines removed for each grain size distribution is given in Table 2. The KC model prediction is significantly improved with a rather modest amount of fines removed from each of the grain size distributions. Besides 70% Rubble samples, the amount removed for each grain size distribution is in the same range (on the order of 5%). The coarser the samples, the larger the particles are that are removed to improve the KC prediction. The method for removing different amounts of particles is by visual inspection of the results relative to the prediction rather than some optimization method. The removal was therefore limited to entire sieve sizes rather than some calculated weight or fraction of salt retained in a sieve. Since the removal of fines from the 70% Rubble model did not have a target permeability, the model was adjusted to approximately the maximum measurable permeability around the range of porosities measured for these samples.

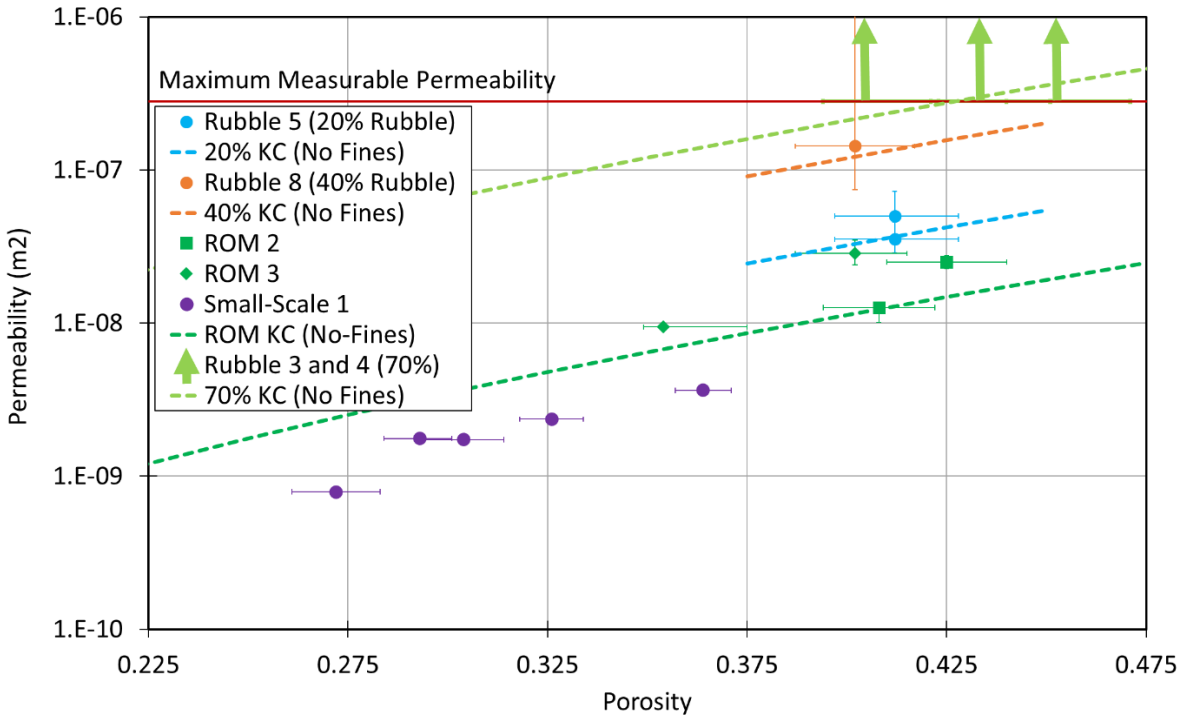

Figure 19: Permeability vs. porosity data with adjusted Kozeny-Carman predictive models for each of the three grain size distributions without the fraction by weight of fines included in the specific surface area estimation sum.

Table 2: Removal of Fines from the KC Model Prediction

Grain Size Distribution	Pertaining Samples	Standard Sieve Size for Which Particles Passing are Removed	Fraction of total Mixture Weight Removed (%)
100% ROM	ROM 2 and 3, Small-Scale 1	#200 (0.075 mm)	6.6
20% Rubble, 80% ROM	Rubble 5	#100 (0.15 mm)	3.8
40% Rubble, 60% ROM	Rubble 8	#50 (0.3 mm)	4.9
70% Rubble, 30% ROM	Rubble 3 and 4	#100 (0.15 mm)	1.4

4.2 Stability Analysis

4.2.1 Kenny and Lau Theory and Derivation

A phenomenon commonly observed in granular mixtures and analyzed in the design of earth dams and filters is mixture instability. In 1985, Kenny and Lau proposed a commonly used method to analyze filters and predict which particles in a grain size distribution may be unstable and lost from the mixture upon exposure to fluid flow through the porous media (Kenny and Lau 1985). The method proposed to measure instability stems from the theory that finer particles can pass through connected void spaces created by larger particles. If voids are created by particles four times larger than a finer particle, it can allow these finer particles to pass through their

constrictions and the stability of these particles is dictated by the number of particles existing between these two particle sizes. For instance, for a particle size D, the constrictions of interest for which they may pass through are created by particles of size equal to 4D. A parameter H is calculated as the mass fraction of particles between the sizes D and 4D to quantify the particles that prevent instability. The second parameter, F, which is the mass fraction of particles smaller than D, is then calculated across the entire grain size distribution to be compared with an empirical stability criterion developed by Loebotsjkov in 1969.

4.2.2 Unstable Particle Sizes

For the Kenny and Lau stability analysis applied to the grain size distributions used in this study, the particle sizes that may be expected to move out of the mixture and not affect the measured permeability may be predicted. The movement of unstable particles may be a similar mechanism as the settling that is suspected in the testing of granular salt with a large particle size range. Results from the stability analysis can be found in Appendix B and indicate that particles smaller than 0.3 mm are expected to be unstable for the grain size distributions: 100% ROM, 20% Rubble, and 40% Rubble. This particle size is the largest size of particles that were removed in section 4.1 from the KC model. Since the removal of these fines from the KC predictive model could represent particle instability, this stability analysis serves to further justify the KC model adjustments made and described in the previous section.

Particle instability as a direct result of rubble is observed in the results of this stability analysis when applied to the 70% Rubble particle size distribution. This stability analysis indicates that particles smaller than the 6.35 mm sieve may be unstable, and reveals that with

enough rubble particles, the larger particles may also cause settlement. However, having the same size of particles (0.3 mm) expected to be unstable for each of the other three grain size distributions indicates that the instability could be induced by the larger particle sizes in ROM salt, since the three samples all contain some ROM salt. This could also indicate that the larger particles in the rubble are not the only cause for the possible settlement of fines, and that the ROM salt may also be responsible for some of the settlement.

4.3.3 Unstable Particle Removal

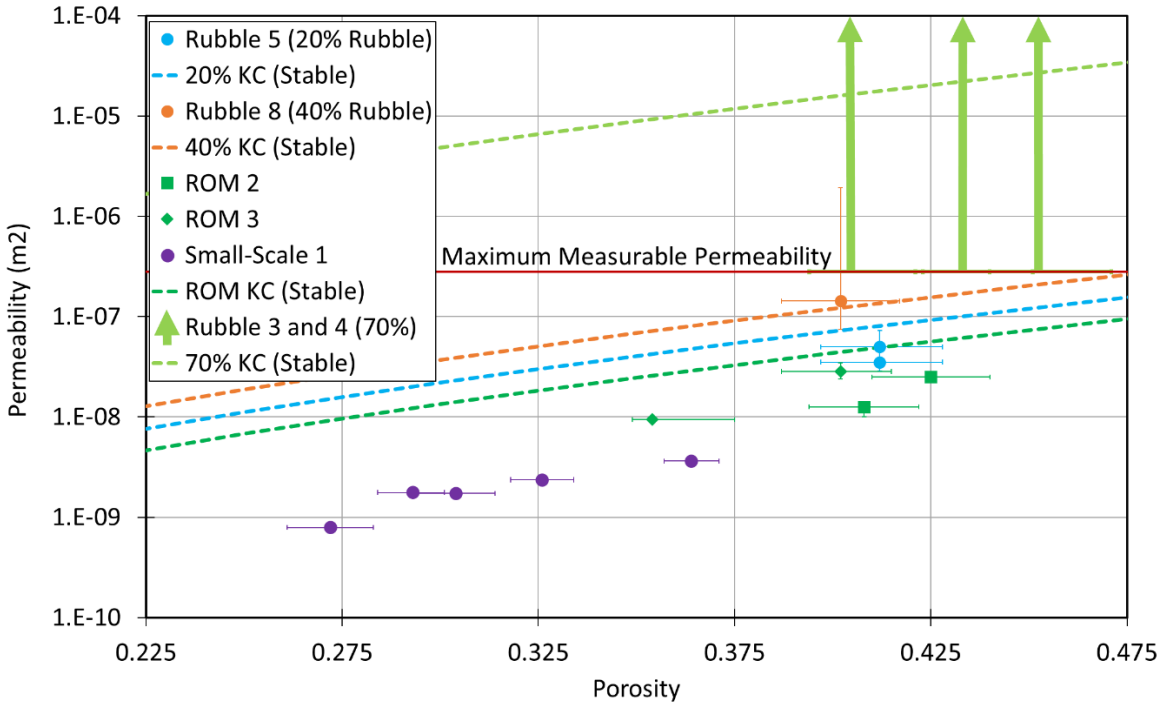

Figure 20: KC predictive model with all particles determined to be unstable by the Kenny and Lau stability analysis removed from the model.

Since the Kenny and Lau stability analysis is just a prediction of which particles in a mixture may be unstable, the analysis does not explicitly mean that these particles will in fact be

unstable. However, looking at the KC prediction with all the particles expected to be unstable removed, as shown in Figure 20 above, reveals that this model overpredicts permeabilities measured for every sample except for the 40% Rubble. This suggests that some of the particles expected to be unstable in this analysis may not be. One possible cause is that the stability analysis does not consider the length of sample which the particles must be filtered out of. It is possible that many of these particles may settle within samples to a certain degree while not completely being filtered out to the bottom of samples.

5. CONCLUSION

5.1 Experimental Configuration Development

An objective of this work was to develop a system to measure permeability and porosity of salt rubble with as large of particle sizes as possible to simulate WIPP roof falls. This objective presents a host of challenges.

First, a large vessel or container for the salt samples was required. Typical guidance is that the diameter of a permeameter should be >~5 times the largest particle diameter. Therefore, a typical cylindrical vessel for conventional laboratory permeability testing would only suffice for the smaller grained salt mixtures such as ROM. For the larger grain sizes intended to be used in this study, a large deck box and sealed bag configuration was developed to allow for accommodating salt particles as large as 25.4 cm in size. At the same time, the size of the box was constrained as the configuration had to be small enough to fit into a CT scanner for further analysis. This constraint also restricted the use of metal in the experimental configuration and is the reason so many parts are made of plastic or wood. This is also the reason that the metal measurement devices such as pressure gages can easily be removed from the sample.

The permeability measurements were made with air under vacuum. By using gas, solubility issues associated with salt were avoided. Vacuum rather than positive gas pressure was used so that the sample could be confined in a sealed polyethylene bag. Under vacuum, the bag conforms to the irregular shape of the salt particles and prevents bypass during the permeability test. Sealing the bag, especially adjacent to the perforations, was very challenging and often required numerous attempts to achieve an adequate seal. The bag is lined with impermeable neoprene sheeting to give it extra deformability and puncture resistance. The permeability

measurement was made by applying vacuum to one end and drawing atmospheric air through the sample. The flowrate and pressure drop in the sample were monitored. To measure porosity, a supplement gas reservoir was introduced into the system to allow for porosity measurements to be made with the gas expansion method. Due to resolution and ranges of different measurement devices, the maximum measurable permeability is 2.80E-7 m^2 and the minimum measurable permeability is 1.08E-12 m^2.

5.2 Permeability and Porosity Relationship

5.2.1 What Trends Are Observed in This Relationship?

In general, for porous media, permeability is expected to increase with increasing porosity. This trend is clearly seen with samples comprised of ROM salt, including samples that were purposefully densified to decrease porosity and permeability.

The permeabilities of the samples containing rubble increase with increasing rubble content, but the porosities are in the same range of between 0.40 and 0.415. Further, attempts to densify the samples with rubble did not change the porosity. Consider the two measurements on sample Rubble 5: the same porosity was found but noticeably different permeabilities before and after shaking in an attempt to densify. This result is contrary to what was measured in ROM samples because ROM samples are expected to contain relatively more homogeneous distributions of particle sizes. Since rubble has such large particles capable of creating much larger pore structures relative to the fine particles, these fines are much more likely to settle and create more heterogeneous mixtures in rubble samples than in ROM samples.

5.2.2 KC Predictive Model Results

The experimental results were compared to predictions from the Kozeny Carman model. Using the Carrier version of the KC model that accounts for the particle size distribution, predictions were lower than the measured permeabilities but within about an order of magnitude. The discrepancy between the measurements and predictions may arise from the role of the finest fraction of the grain size distribution. In the model, the finest fraction has a large impact on the predicted permeability as it contributes significantly to the specific surface area term in the model. In the measurements, it is suspected that there is not enough of the finest fraction to be distributed uniformly within the flow cross-section sample and therefore not necessarily involved in flow. In other words, relatively large voids will remain that will dominate flow. Further, the finest fraction may settle (inadvertently but also during densification efforts) and effectively stratify the sample. Using the Kenny and Lau stability analysis, the fraction of the sample predicted to be unstable and hence prone to settling was determined. The results of this analysis correlated with the empirical (visual inspection) adjustment of the KC model since the unstable particles may not contribute to the permeability of a sample. Removing some or all of this fraction of unstable particles from the grain size distribution used in the KC model resulted in improved predictions.

5.3 Future Work

5.3.1 Further Analysis of Results and Models

Additional model development or modification should be considered in order for predictions to better match experimental results reported here. Additional tests of rubble samples

at different levels of densification could reveal trends in the relationship with the KC predictive model.

5.3.2 Analysis of CT Images

One of the challenges of this study was to create an experimental configuration capable of being CT scanned. While the Rubble 5 salt sample was CT scanned towards the end of the duration of this study, the data collected from the scan was not yet available at the time this document was completed. Continuing this research would certainly include the analysis of these images once they are presentable.

Since the CT scan is meant to map the pore space throughout the sample, it is expected that the images would reveal how the salt grains within samples are arranging themselves. One of the unanswered questions of this study is how the fines in samples may be settling withing the pore structure? How are fines arranging themselves and is it in a way that may cause them to have little to no impact on the measured permeability of the sample? These questions are among many that the data from these CT scans may help answer.

5.3.3 Large-Scale Permeability Testing with Vertical and Horizontal Flow

Related to the way fines are arranging themselves in samples is the possible difference between the horizontal and vertical permeabilities of a sample. If fines are settling to the bottom of the entire sample or to the bottom of large pores within a sample, the horizontal permeability is expected to be larger than the vertical permeability. In continuing this research, the alteration of the experimental configuration to simultaneously measure vertical and horizontal permeability

of a sample would be valuable for the analysis of this effect. A similar inserted pipe configuration along the side of salt samples could be used to accomplish measuring both horizontal and vertical permeability of a sample.

5.3.4 Diffusion Testing

Both gas diffusion and heat diffusion can be envisioned as relevant transport mechanisms for rubble from roof falls in a nuclear waste repository. Gas diffusion could be measured in the permeameter configuration with some modifications. However, obtaining data from gas diffusion-only transport is not straightforward because it is very difficult to completely exclude advective flow when the permeability of the sample is so large. In a similar manner, isolating diffusive and convective heat flow is very challenging in materials with such large permeabilities.

6. APPENDICES

A: Unsuccessful Sample Information

B: Exact Permeability and Porosity Measurements

C: Non-linear Flow Correction Plots for Permeability Measurements

D: Kenny and Lau Stability Analysis Results

A: Unsuccessful Sample Information

The following section describes salt samples in addition to Section 3.1.1 and quantifies their key parameters in addition to Table 1 in section 2.8.8.

Table 3: Unsuccessful WIPP Salt Samples Tested and Their Key Parameters

Name Date Constructed	Experimental Configuration	Grain Size Distribution	Vibration Method	Approx. Leak Rate (kPa/s)
ROM 1 1/21/2021	Permeameter (1.2 m box)	100% ROM	Rolling on Pavement	>0.01, (0.755 SLPM)
Rubble 1 5/7/2021	Permeameter (1.2 m box)	70% Rubble (Up to 40 cm chunks)	Rolling on Pavement	>0.01, (0.999 SLPM)
Rubble 2 7/1/2021	Permeameter (1.2 m box)	70% Rubble (Up to 40 cm chunks)	Rolling on Pavement	0.00090, (0.093 SLPM)
Rubble 6 12/9/2021	Permeameter (1m box)	40% Rubble (Up to 25 cm), 60% ROM	None	0.0043, (0.402 SLPM)
Rubble 7 12/22/2021	Permeameter (1m box)	40% Rubble (Up to 25 cm), 60% ROM	None	0.0043, (0.414 SLPM)

The first two samples built in this study, ROM 1 and Rubble 1, were tested with different measurement devices as briefly described in section 2.4. Throughout the testing of ROM 1 and Rubble 1, the flow measurements were made using rotameters which proved to have low resolution and accuracy. However, the rotameters gave an idea of the range of flowrates expected

from samples and allowed for the correct range mass flowmeter to be implemented in testing of future samples. Additionally, pressure measurements made on these two samples were inaccurate. Due to uncalibrated pressure gauges, differential pressures appeared to be much larger than they really were. Until the Dwyer differential pressure gauge was implemented in ROM 2, the fact that these pressure gauges could not accurately resolve the differential pressure across these samples was unknown and permeability calculations for these two samples were severely underestimated.

Data from Rubble 2, 3, and 4 are only partially presented because their permeabilities were too large to measure with the methods and measurement devices used in this study. The resolution and range of the measurement devices limits permeability measurements to an upper bound of $2.8 \times 10^{-7} m^2$ as shown by the dark red line in Figure 13. Since Rubble 2, 3, and 4 all contain 70% rubble in their grain size distributions, their permeabilities are expected to be relatively large with respect to other samples such as Rubble 8 which approaches the maximum measurable permeability. During the testing of these three samples, the differential pressure gauge was unable to resolve a differential pressure measurement, and permeability calculations could not be completed as a result. For Rubble 3 and 4, porosities were measured and shown in Figure 16. Since the permeabilities are concluded to be at or above the resolution, these data points are given by arrows stretching above the maximum measurable permeability line. No porosity was measured for Rubble 2 since the sample was determined to be rebuilt at the time following the inconclusive permeability test.

Data from Rubble 6 and 7 are not presented because of excess leakage into the sealed plastic bag. Rubble 6 and 7 were the first and second attempts at creating a sample containing

60% ROM and 40% rubble in their grain size distributions. The leak rate in the sealed plastic bags were determined to be too large and warranted the reconstruction of the sample with the same salt. As a result, Rubble 8 was the first sufficiently sealed sample to contain this same particle size distribution.

B: Exact Permeability and Porosity Measurements

Exact values of permeability and porosity measured as presented graphically in sections 3 and 4.

Table 4: Successful Permeability and Porosity Measurements Made

Sample Name	Trial	Permeability (m^2)	Porosity
ROM 2	1 (Before shaking)	2.50E-8	0.425
	2 (After shaking)	1.26E-8	0.408
ROM 3	1 (Before shaking)	2.84E-8	0.402
	2 (After shaking)	9.41E-9	0.354
Small-Scale 1	1 (Before shaking)	1.73E-9	0.304
	2 (After shaking)	7.89E-10	0.272
	3 (Salt placement reset before shaking)	3.63E-9	0.364
	4 (Salt placement reset after shaking)	2.36E-9	0.326
	5 (Salt placement reset after shaking twice)	1.76E-9	0.293
Rubble 3	1 (Before shaking)	Immeasurable	0.453
	2 (After shaking)	Immeasurable	0.434
Rubble 4	1	Immeasurable	0.405
Rubble 5	1 (Before shaking)	3.52E-8	0.411

	2 (After shaking)	7.23E-8	0.412
Rubble 8	1	1.43E-7	0.402

C: Non-linear Flow Correction Plots for Permeability Measurements

Non-linear flow correction plots for successful permeability tests. Each non-linear flow correction utilizes 5 or more apparent permeability measurements to calculate the corrected permeability as discussed in section 2.5.1.

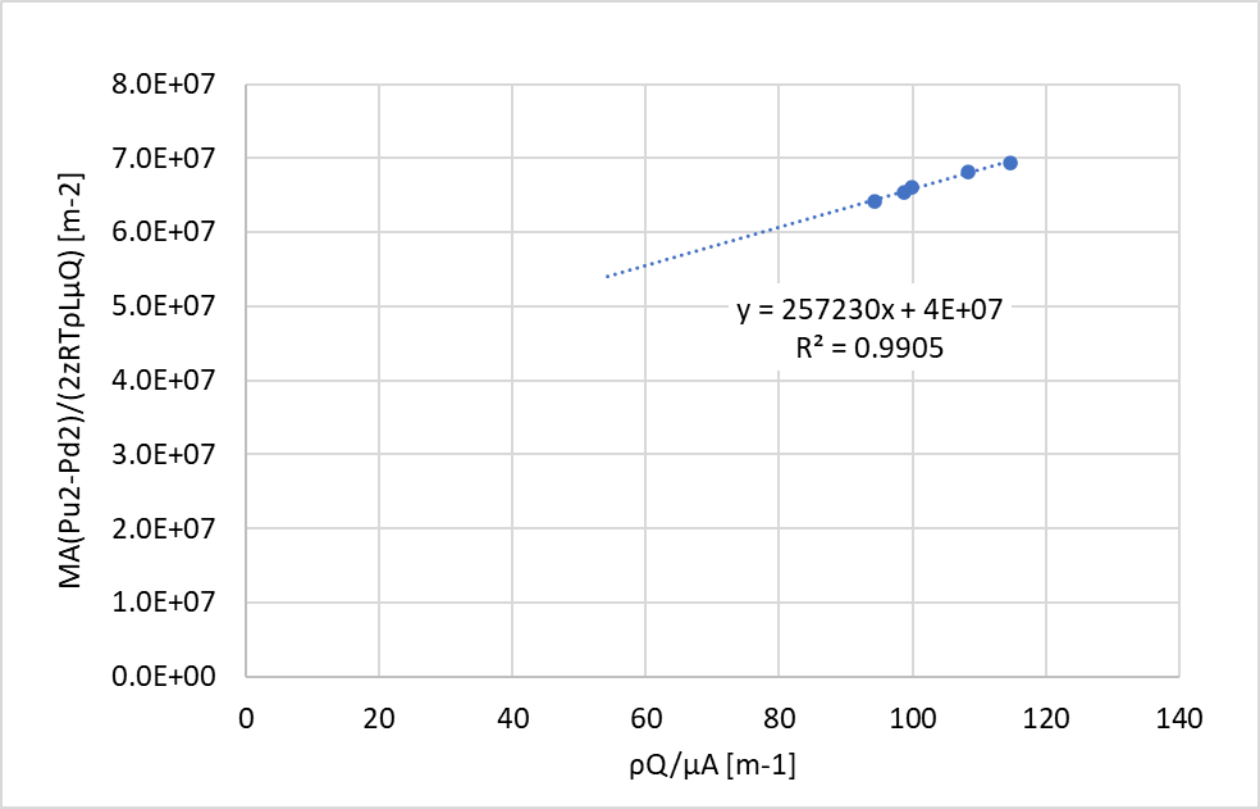

Figure 21: Non-linear flow correction for ROM 2 before shaking. Measurements made on June 21st, 2021.

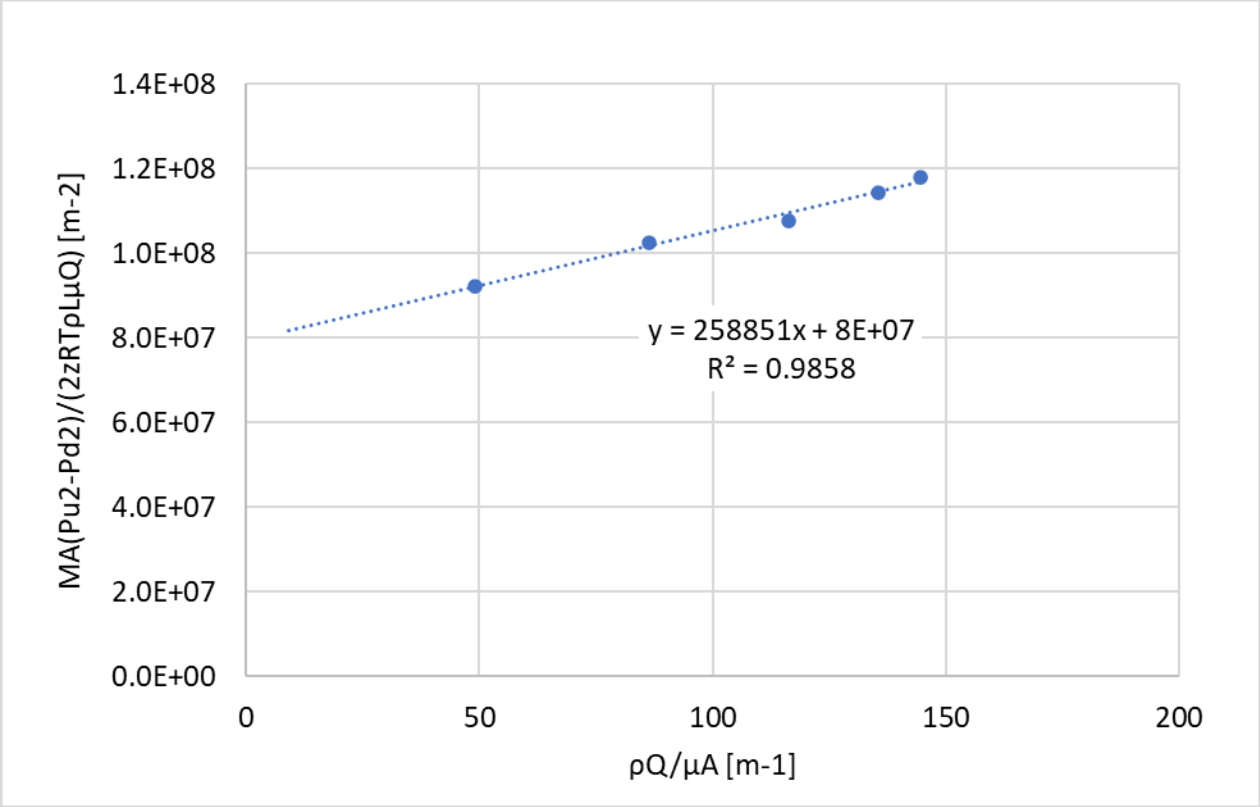

Figure 22: Non-linear flow correction for ROM 2 after shaking. Measurements made on June 23rd, 2021.

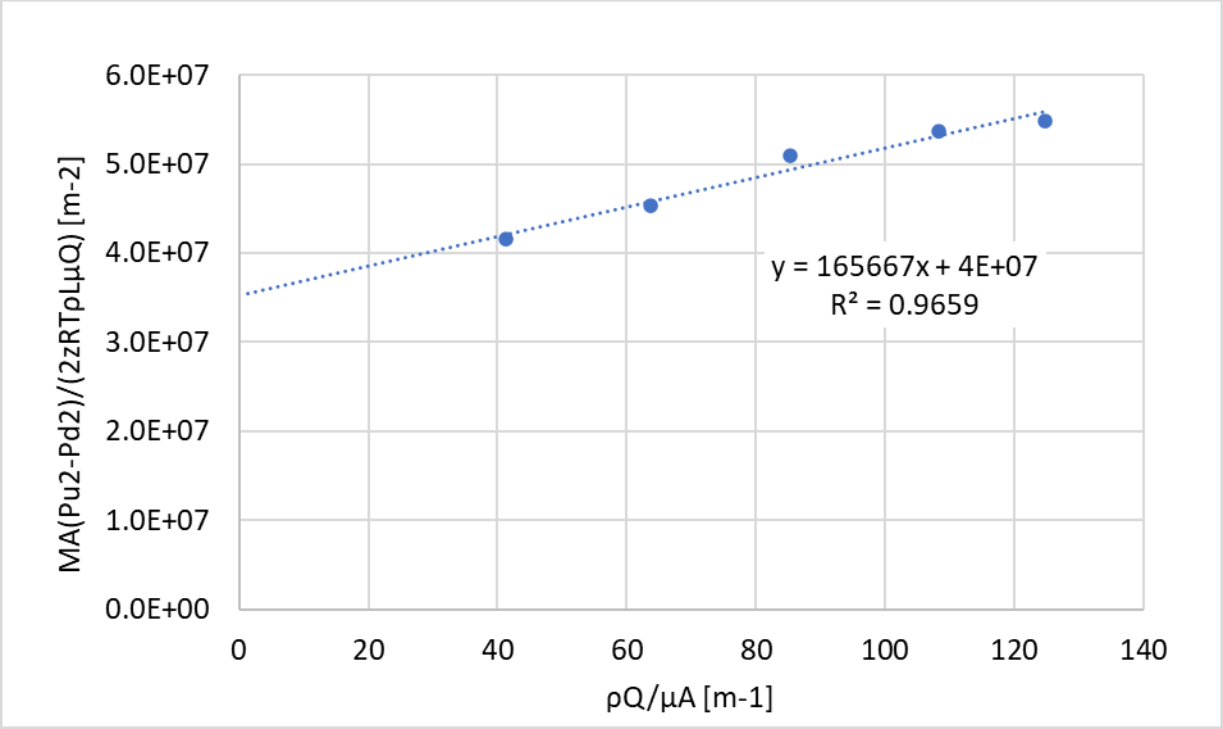

Figure 23: Non-linear flow correction for ROM 3 before shaking. Measurements made on August 26th, 2021.

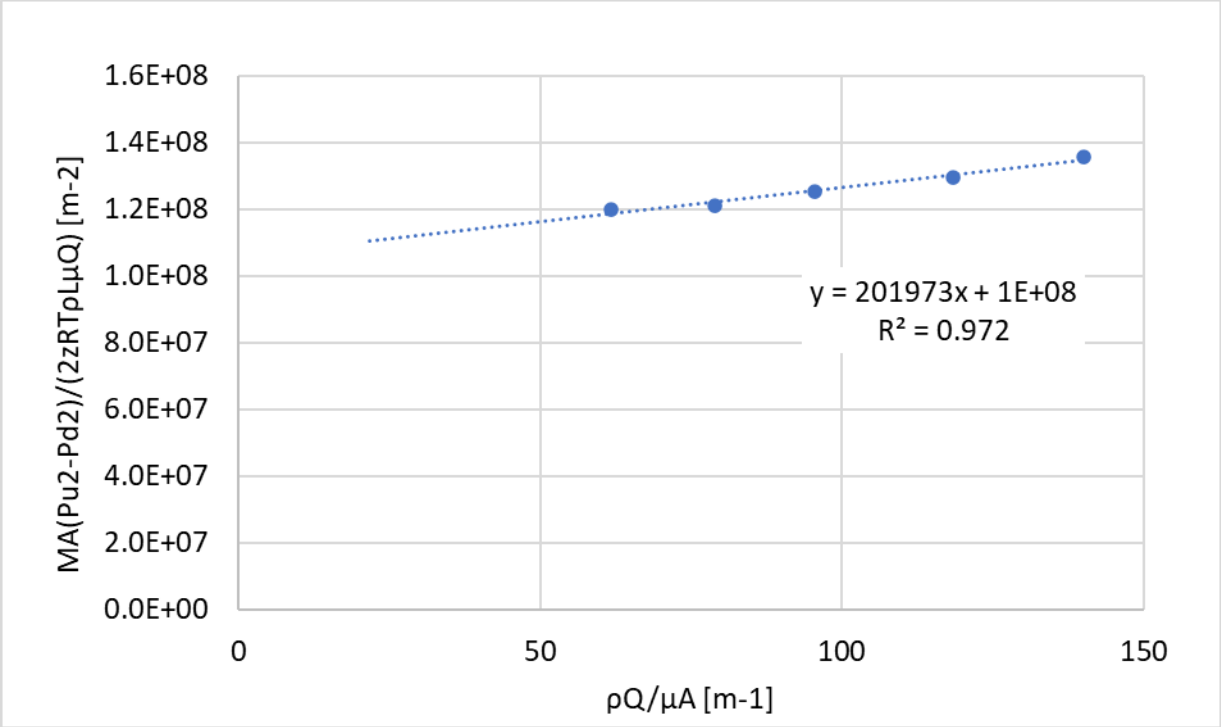

Figure 24: Non-linear flow correction for ROM 3 after shaking. Measurements made on September 1st, 2021.

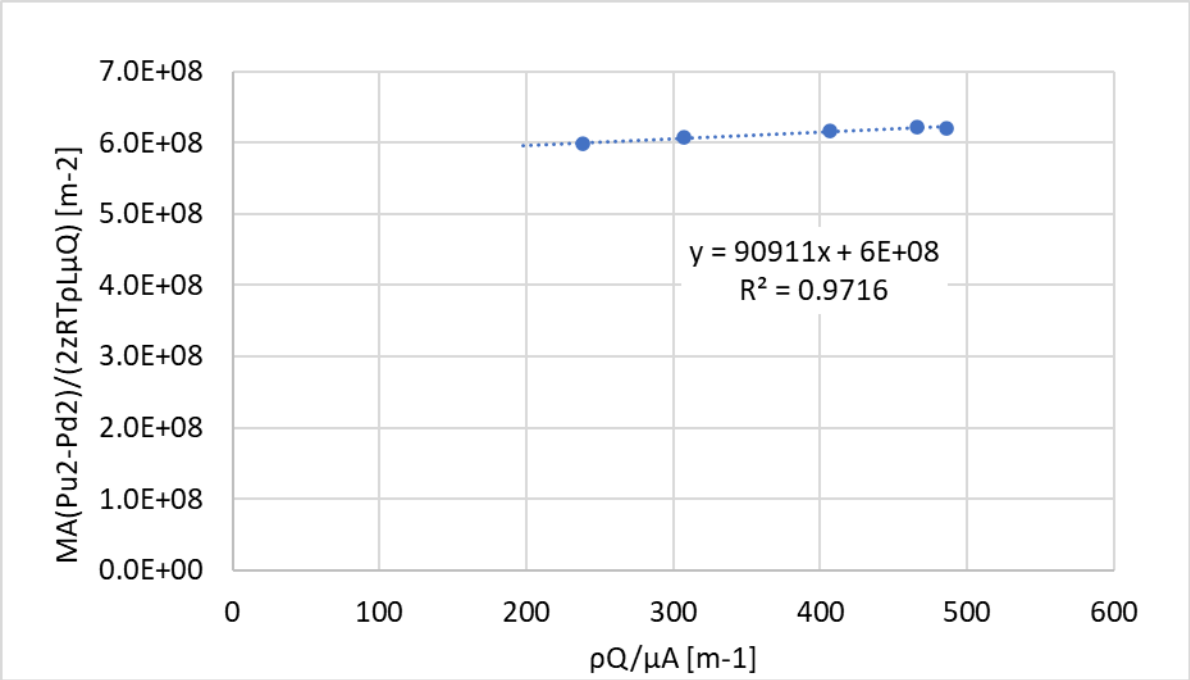

Figure 25: Non-linear flow correction for Small-Scale 1 before shaking. Measurements made on September 29th, 2021.

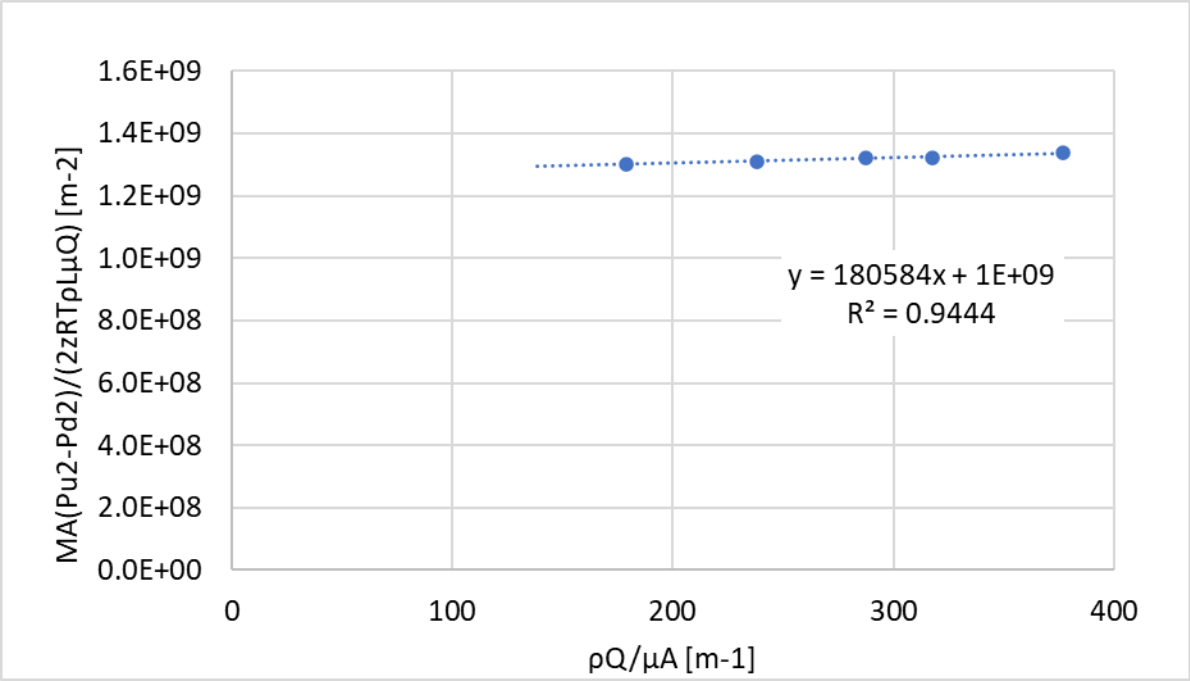

Figure 26: Non-linear flow correction for Small-Scale 1 after shaking. Measurements made on October 5th, 2021.

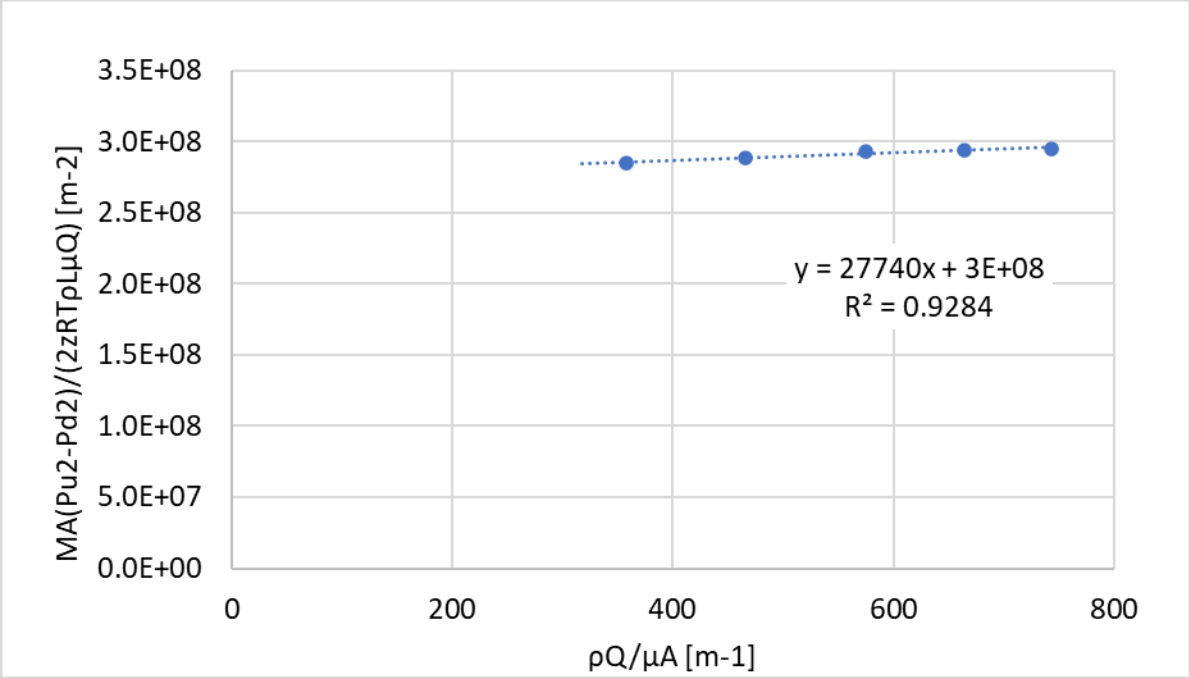

Figure 27: Non-linear flow correction for Small-Scale 1 after salt placement reset and before shaking. Measurements made on October 6th, 2021.

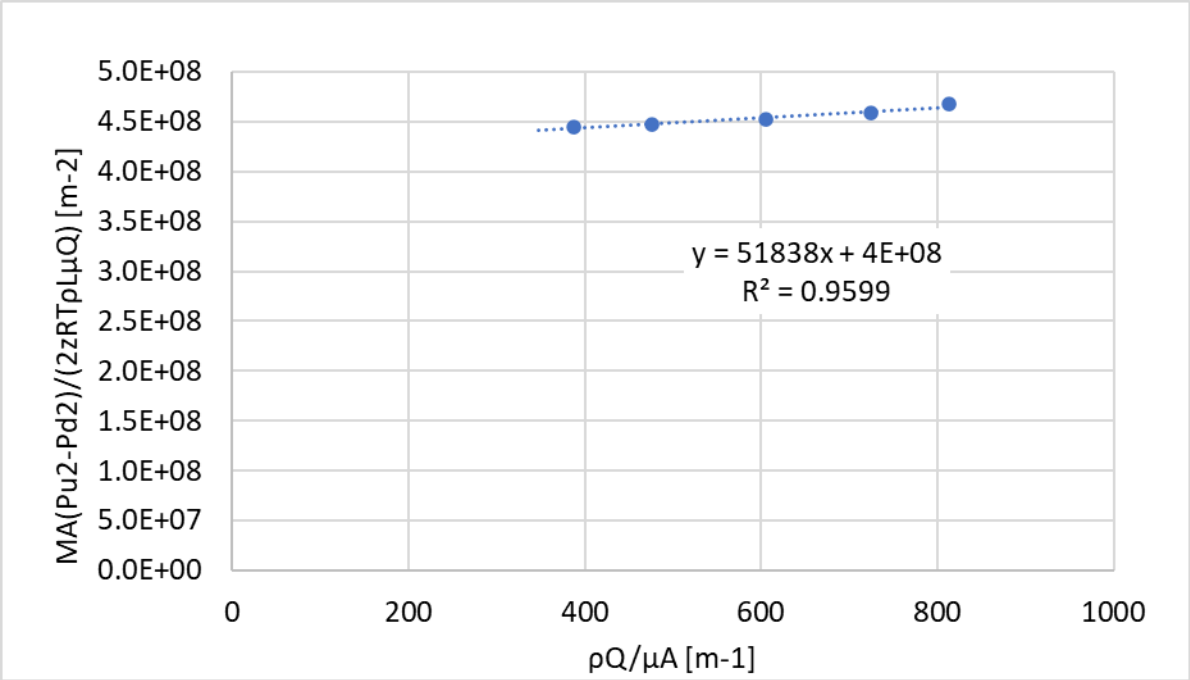

Figure 28: Non-linear flow correction for Small-Scale 1 after salt placement reset and after shaking. Measurements made on October 6th, 2021.

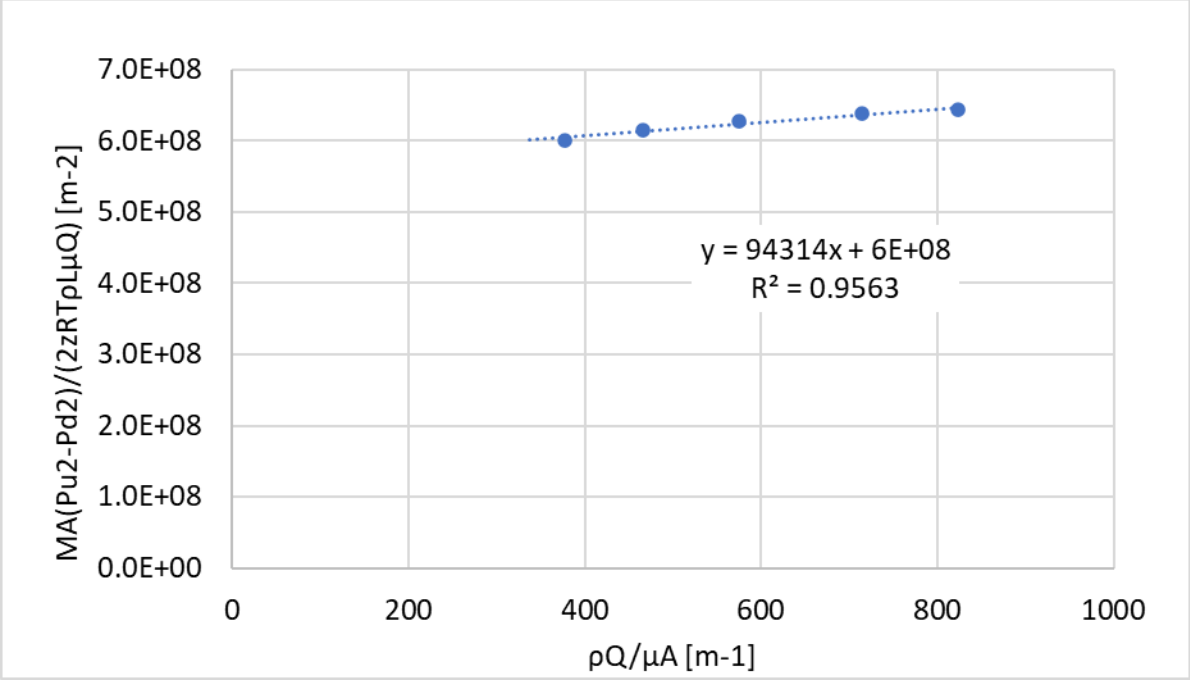

Figure 29: Non-linear flow correction for Small-Scale 1 after salt placement reset and after shaking twice. Measurements made on October 6th, 2021.

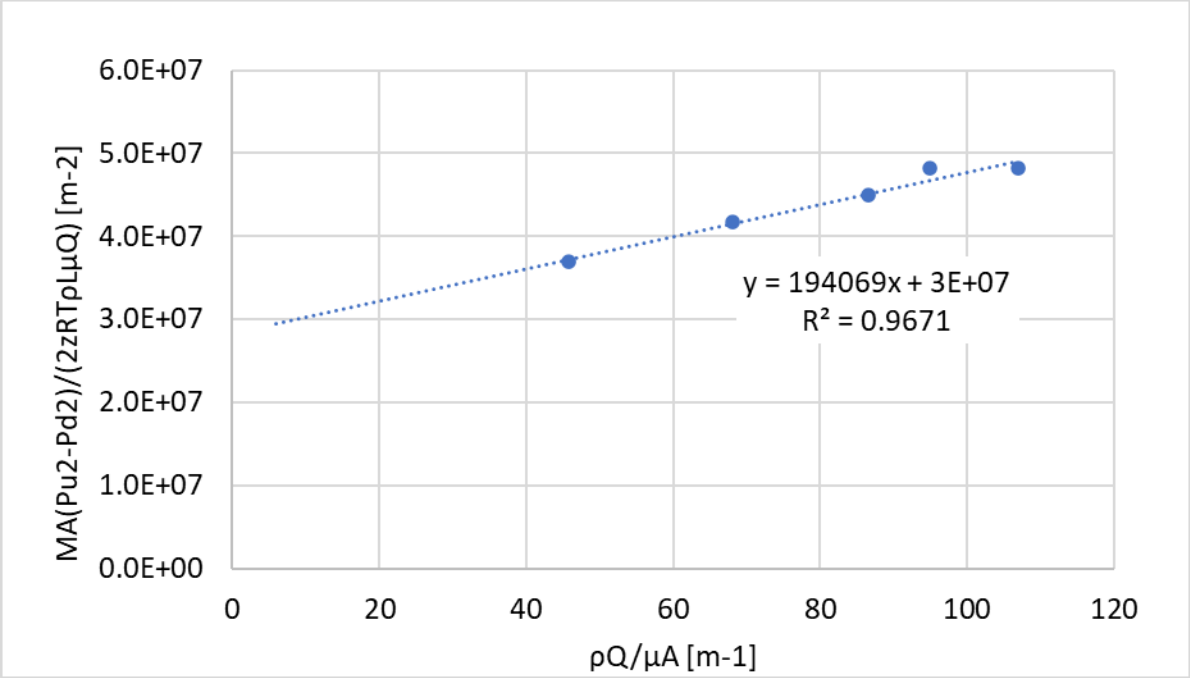

Figure 30: Non-linear flow correction for Rubble 5 before shaking. Measurements made on November 8th, 2021.

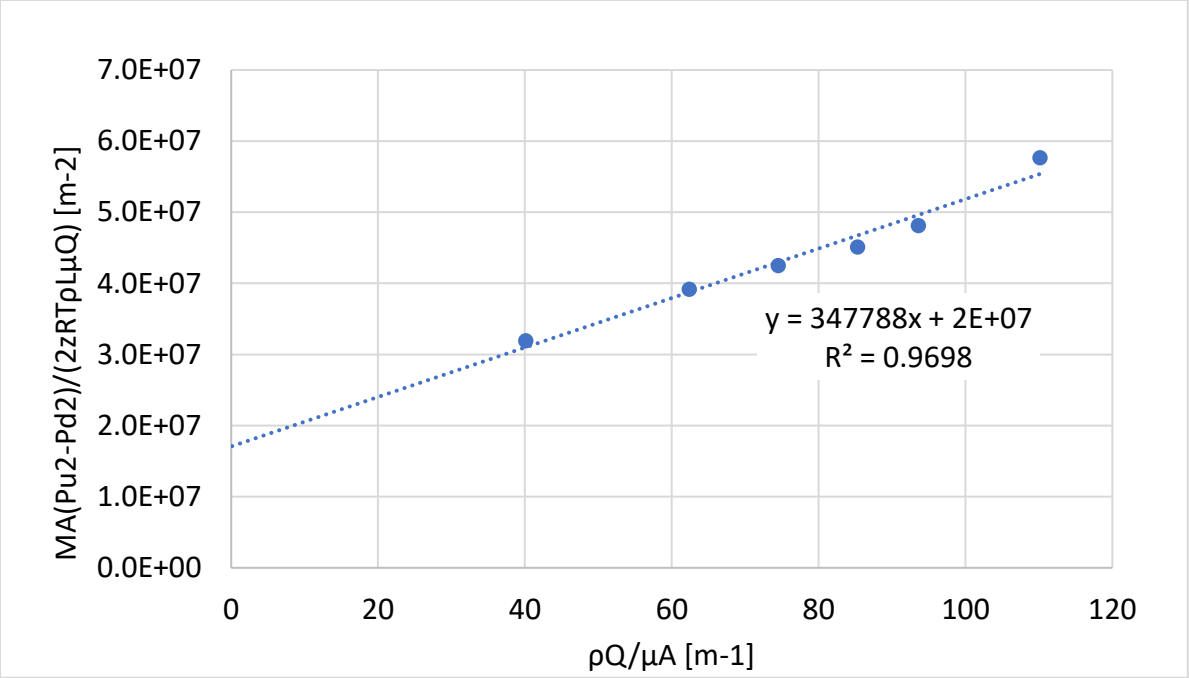

Figure 31: Non-linear flow correction for Rubble 5 after shaking. Measurements made on May 2nd, 2022.

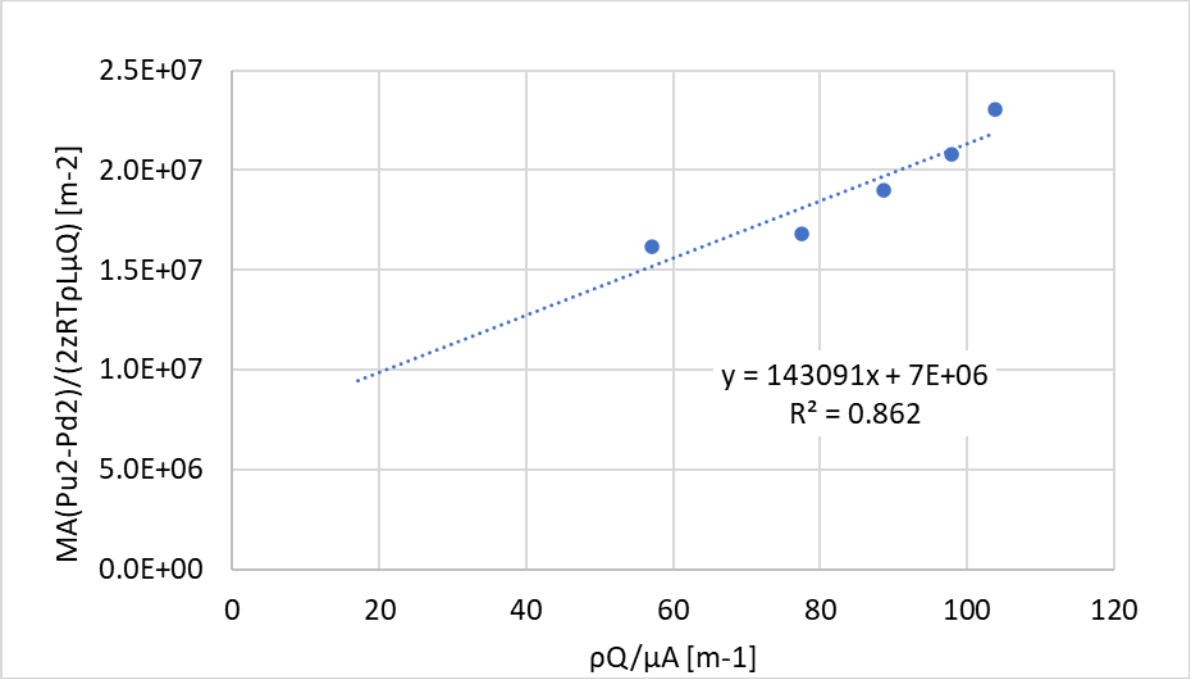

Figure 32: Non-linear flow correction for Rubble 8. Measurements made on February 1st, 2022.

D: Kenny and Lau Stability Analysis Results

Results of the Kenny and Lau stability analysis. As described in section 4.2, each particle size distribution has a separate stability analysis and this section shows the results from the four particle size distributions: 100% ROM, 20% Rubble, 40% Rubble, and 70% Rubble. Each result plot includes a shape curve, or "F-H curve" calculated from the grain size distribution, a stability criterion curve equal to H=1.3F, and a boundary curve equal to F+H=1. For particles to be unstable, the shape curve must fall below the stability criterion curve a mass fraction value smaller than 0.2 for widely graded distributions. In this study, all 4 particle size distributions were calculated to be widely graded.

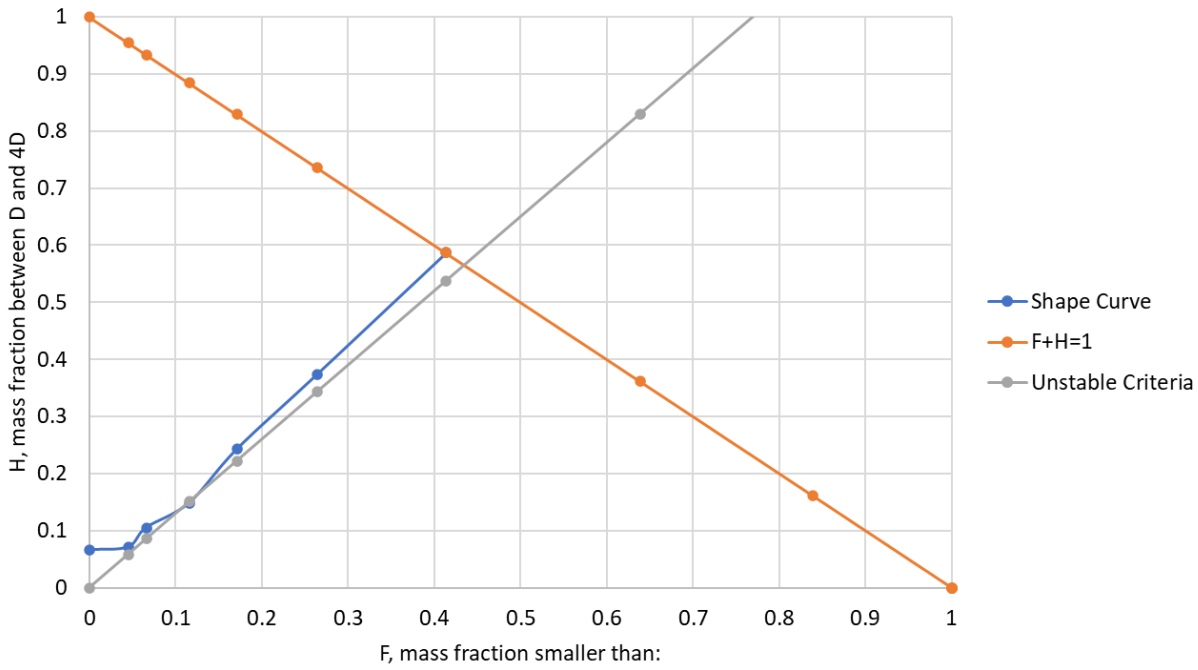

Figure 33: Kenny and Lau stability analysis plot for the particle size distribution: 100% ROM.

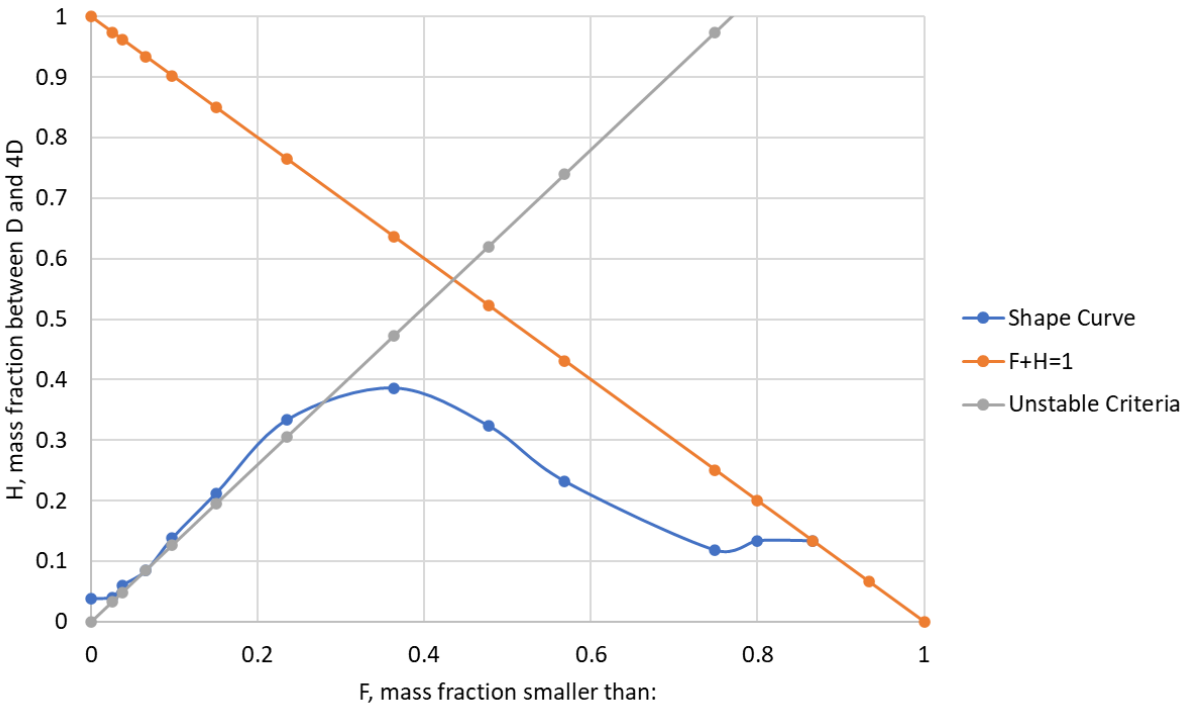

Figure 34: Kenny and Lau stability analysis plot for the particle size distribution: 20% Rubble.

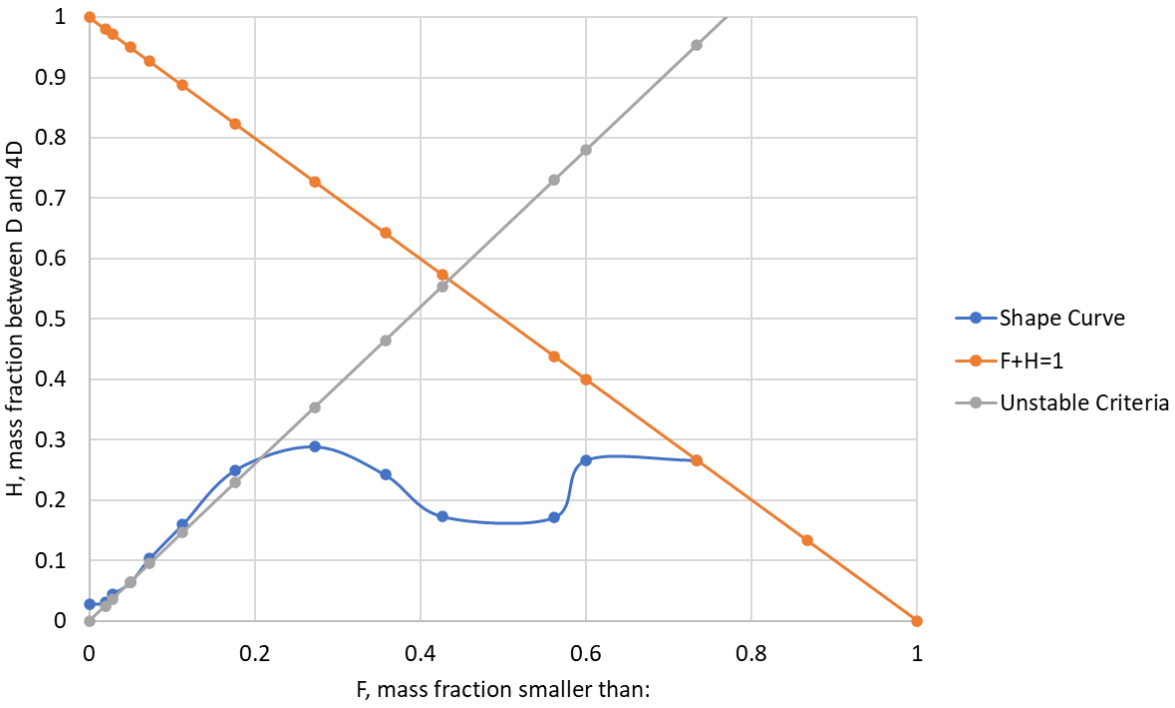

Figure 35: Kenny and Lau stability analysis plot for the particle size distribution: 40% Rubble.

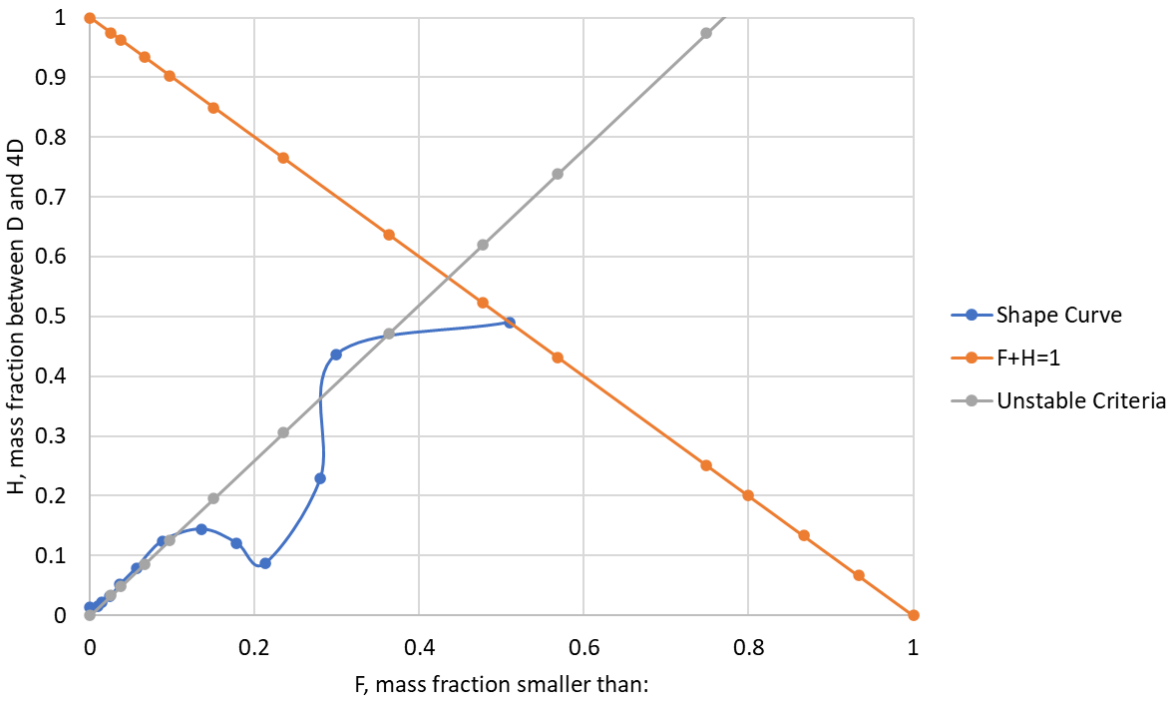

Figure 36: Kenny and Lau stability analysis plot for the particle size distribution: 70% Rubble.

7. REFERENCES

1. *Backgrounder on radioactive waste | NRC.GOV - NRC web*. United States Nuclear Regulatory Commission. (n.d.). Retrieved February 1, 2022, from https://www.nrc.gov/reading-rm/doc-collections/fact-sheets/radwaste.html
2. Bechthold, W., & Bollingerfehr, W. (2002). Backfilling and sealing of underground repositories for radioactive waste in salt, Phase II (BAMBUS project). *Europace*.
3. Borns, D. J., & Stormont, J. C. (1988). Interim report on excavation effect studies at the Waste Isolation Pilot Plant: The delineation of the Disturbed Rock Zone. *International Journal of Rock Mechanics and Mining Sciences & Geomechanics Abstracts*, *27*(4). https://doi.org/10.1016/0148-9062(90)90963-3
4. Borns, D. J., & Stormont, J. C. (1990). Delineation of the disturbed rock zone surrounding excavations in Salt. *International Journal of Rock Mechanics and Mining Sciences & Geomechanics Abstracts*, *27*(2). https://doi.org/10.1016/0148-9062(90)95353-3
5. Brodsky, N. S. (1994). Hydrostatic and shear consolidation tests with permeability measurements on waste isolation pilot plant crushed salt. https://doi.org/10.2172/10142397
6. Carrier, W. D. (2003). Goodbye, Hazen; Hello, Kozeny-Carman. *Journal of Geotechnical and Geoenvironmental Engineering*, *129*(11), 1054–1056. https://doi.org/10.1061/(asce)1090-0241(2003)129:11(1054)
7. Chan, K. S., Bodner, S. R., & Munson, D. E. (2001). Permeability of wipp salt during damage evolution and healing. *International Journal of Damage Mechanics*, *10*(4), 347–375. https://doi.org/10.1106/h3uv-1ura-afuy-fx49

8. Chapuis, R. P. (2012). Predicting the saturated hydraulic conductivity of soils: A Review. *Bulletin of Engineering Geology and the Environment*, *71*(3), 401–434. https://doi.org/10.1007/s10064-012-0418-7

9. Cinar, Y., Pusch, G., & Reitenbach, V. (2006). Petrophysical and capillary properties of compacted salt. *Transport in Porous Media*, *64*(2), 199–228. https://doi.org/10.1007/s11242-005-2848-1

10. The current bases for roof fall prediction at WIPP and a preliminary prediction for SPDV room 2. (1993). https://doi.org/10.2172/10191310

11. Ezersky, M., & Goretsky, I. (2014). Velocity–resistivity versus porosity–permeability inter-relations in Dead Sea Salt Samples. *Engineering Geology*, *183*, 96–115. https://doi.org/10.1016/j.enggeo.2014.09.009

12. Fair, G. M., & Hatch, L. P. (1933). Fundamental factors governing the streamline flow of water through sand. *Journal - American Water Works Association*, *25*(11), 1551–1563. https://doi.org/10.1002/j.1551-8833.1933.tb18342.x

13. Hansen, F. D., Steininger, W., & Bollingerfehr, W. (2017). Proceedings of the 7th US/german workshop on Salt Repository Research, design, and Operation. https://doi.org/10.2172/1432286

14. History of the strategic petroleum reserve. Energy.gov. (2015, July 1). Retrieved February 15, 2022, from https://www.energy.gov/articles/history-strategic-petroleum-reserve

15. Kenney, T. C., & Lau, D. (1985). Internal stability of granular filters. *Canadian Geotechnical Journal*, *22*(2), 215–225. https://doi.org/10.1139/t85-029

16. Krohn, K.-P., Zhang, C. L., Wolf, J., Stuhrenberg, D., Jobmann, M., Borstel, L. von, & Lerch, C. (2012). The compaction behaviour of salt backfill at low porosities. *Mechanical Behaviour of Salt VII*, 175–182. https://doi.org/10.1201/b12041-24

17. Matteo, E. N., Mitchell, C., & Dewers, T. A. (2020). Characterization of Permeability/Porosity Relationships as a Function of Rubble Pile Polydispersity during Room Closure at the Waste Isolation Pilot Plant. *American Rock Mechanics Association*.

18. National Academy of Sciences- National Research Council (1957). The disposal of radioactive waste on land. Publication 519. Washington, D.C.

19. National Research Council. (2001). Improving operations and long-term safety of the Waste Isolation Pilot Plant. https://doi.org/10.17226/10143

20. Powers, D. W., Lambert, S. J., Shaffer, S. E., & Hill, L. R. (1978). Geological characterization report, waste isolation pilot plant (WIPP) site, southeastern New Mexico. https://doi.org/10.2172/6441454

21. Reedlunn, B., Moutsanidis, G., Baek, J., Huang, T.-H., Koester, J., Matteo, E., He, X., Taneja, K., Wei, H., Bazilevs, Y., Chen, J.-S., Mitchell, C., Lander, R., & Dewers, T. (2019). Initial simulations of empty room collapse and reconsolidation at the Waste Isolation Pilot Plant. https://doi.org/10.2172/1592852

22. Spangenberg, E., Spangenberg, U., & Heindorf, C. (1998). An experimental study of transport properties of Porous Rock Salt. *Physics and Chemistry of the Earth*, *23*(3), 367–371. https://doi.org/10.1016/s0079-1946(98)00039-1

23. Storing hydrogen underground. AIS Software. (2017, September 13). Retrieved June 10, 2022, from https://www.aissoftware.com/storing-hydrogen-underground/

24. Stormont, J. C. (1990). Discontinuous behavior near excavations in a bedded salt formation. https://doi.org/10.2172/6461949

25. WIPP. U.S. Department of Energy's Waste Isolation Pilot Plant - Wipp Site. (n.d.). Retrieved March 21, 2022, from https://wipp.energy.gov/wipp-site.asp

26. Zeng, Z., & Grigg, R. (2006). A criterion for Non-Darcy flow in porous media. *Transport in Porous Media*, *63*(1), 57–69. https://doi.org/10.1007/s11242-005-2720-3

27. Ziarani, A. S., & Aguilera, R. (2011). Knudsen's permeability correction for tight porous media. *Transport in Porous Media*, *91*(1), 239–260. https://doi.org/10.1007/s11242-011-9842-6